Alma Mater Studiorum · University of Bologna

School of Science
Department of Physics and Astronomy
Master Degree in Physics

The Effective Field Theory as a searching tool for presence of new physics in $t\bar{t}$ production with CMS

Supervisor:
Prof. Andrea Castro

Submitted by:
Lina Maria Ortiz Parra

Academic Year 2019/2020

Abstract

Despite its success, the standard model (SM) presents some important shortcomings, and because of these there has been a long search for physics beyond the SM which can be associated to the production of a new particle. Since for the moment there is no clear evidence of this we are motivated to use effective field theory to characterise corrections of the Lagrangian of the SM.

The CMS experiment uses the effective field theory (EFT) with four different approaches, based on: 1) the reinterpretation of inclusive measurement, constraining the Wilson coefficient by using EFT parametrizations; 2) relying on reinterpretation of differential measurements at particle and parton level; 3) hybrid EFT measurements at detector level; 4) by characterising EFT directly with the data.

Measurements of top quark $t\bar{t}$ differential cross-sections using simulated events produced in proton-proton collisions are presented. The differential cross-section is defined as a function of kinematic variables for the three decay channels: all-hadronic, semi-leptonic and dileptonic at particle and detector level. The cross-section has been measured for the SM events and EFT using the ctG, cQq81 and ctq8 Wilson coefficients, which were the most relevant. We analyse the different effects that are presented in each channel and also which are the relevant kinematic variables in each case. Based on the differential cross-section histograms we calculate the ratio between EFT and SM production, and analyse the trend of the linear fit in order to see which variables could help us constrain more the Wilson coefficients.

Contents

Chapter 1

Introduction

The standard model (SM) is a relativistic theory of quantum fields, which describes how the elementary particles interact with each other through the electromagnetic, weak and strong force. The discovery of the Higgs boson in 2012 was an additional confirmation of the effectiveness of this model. The Higgs field assigns mass to other particles of the SM through the Higgs mechanism [1]. Despite of the success of the SM, this is not complete because it does not include the gravitational interaction, which is one of the four fundamental forces. It also does not explain why gravity is weaker than electromagnetic or nuclear forces. Another problem of this model is that it assumes that neutrinos do not have mass, but according to the neutrinos oscillation experiment they do have mass [2]. Also, it does not explain the presence of dark matter in the universe and has a hierarchy problem [3]. The major contribution to the mass of the Higgs boson is associated to the loop of the quark top; because the quark top is the most massive particle of the SM, this loop introduces a quadratic divergence at high energies [4].

There are different theories beyond the standard model, BSM that can give a possible solution to these problems, like supersymmetry (SUSY) [5], which extends the number of particles of the SM assigning a superpartner to each particle with the same properties but different spin. Nevertheless, these new particles have not been detected. The absence of this detection could be because the masses of these particles are beyond of our reach. The lack of evidence of BSM physics motivates the use of an effective field theory (EFT) [6]. This theory is characterised by corrections to the SM Lagrangian, which is composed by a series of expansions in the inverse of the energy scale $1/\Lambda$, where Λ is the mass of the new particle. This new Lagrangian will also depend on a dimensionless coupling constant, called the Wilson coefficient, which parameterize the strength of the new physics interactions. This will also have a contribution on the cross-section. The

advantage of EFT is that it provides a framework depending on as few assumptions as possible, with which we can discuss the presence of BSM physics, even if it is associated to particles whose properties are unknown and with mass beyond the energy reach.

In this work we study the contributions of the Wilson coefficients and find which ones gives a larger relative effect to constrain better these coefficients. In order to do this, we measure the $t\bar{t}$ differential cross-section in a p-p collision as a function of a variable for the standard model and the EFT. We do the analysis on top quarks since it is the heaviest known elementary particle and it has the strongest coupling to the Higgs field, therefore, top quarks may play a special role in this search for new physics phenomena. The analysis was made in the three different decay channels: the All-hadronic, semi-leptonic and dileptonic.

For this we generate Monte-Carlo samples for the standard model signal, and EFT process by turning on one coefficient at a time. We use different values of the coefficient to see in which we can obtain a higher cross-section. The analysis has been made at two levels: at particle level and detector level. The simulations where made using MadGraph, which generates the events at parton level. Then we use Pythia, to generate the parton shower and hadronization, and we use Delphes to simulate the detector.

The relevant coefficients are ctG, cQq81 and ctq8, we based our analysis in this three coefficients, since these where the ones that gives a better contribution to the EFT process. The variables of interest for the all-hadronic channel are: the jet multiplicity, the transverse momentum of the leading jet and the THT variable. For the semi-leptonic and dileptonic channel the variables of interest are: the transverse momentum of the lepton and the THT variable.

Chapter 2

Theoretical concepts

2.1 Standard model

The SM is a renormalizable field theory, and its Lagrangian refers to the symmetry group $SU(3) \times SU(2) \times U(1)$, which describes strong, weak and electromagnetic interactions, through the exchange of the corresponding spin-1 gauge fields. The SM classifies the elementary particles in two big families: quarks and leptons. There are six leptons, with spin 1/2, which are classified according to their charge (e or 0), mass and lepton number. They are the electron, muon and tau, plus their corresponding neutrinos. To each lepton corresponds an antilepton with opposite charge and lepton number. There are also six quarks with spin 1/2 and electric charge 2e/3 or $-$e/3. They are named up, down, charm, strange, top and bottom, with a specific flavour quantum number associated to them. To each quark corresponds an antiquark with opposite charge and flavour number. Quarks are bound together to form hadrons, which are classified in baryons, that are made by three quarks, and mesons, made of a quark and an antiquark. Each family is classified in three generation types, where each generation is heavier than the previous one.

The SM also describes three of the four fundamental forces, where each force has its corresponding boson: the strong force is carried by the gluon, the electromagnetic is carried by the photon and the weak force is carried by the charged bosons W^+ and W^- and the neutral boson Z. All the known fundamental particles are shown in Fig. 2.1. Additionally, the Higgs field assigns mass to the other particles of the SM model through the Higgs mechanism.

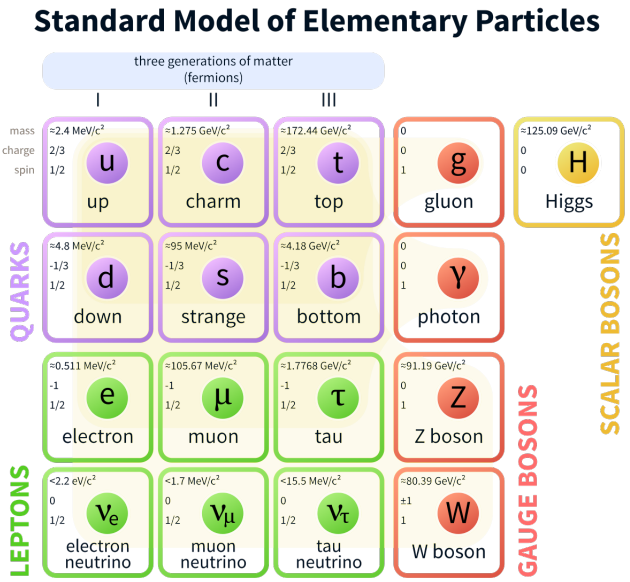

FIGURE 2.1: Particles of the standard model [7]

The Lagrangian of the standard model $\mathcal{L}_{SM}$ can be divided in two parts, one for the strong interaction, described as quantum chromodynamics (QCD), and the other part for the electroweak interaction, so we have:

$$\mathcal{L}_{SM} = \mathcal{L}_{QCD} + \mathcal{L}_{EM}. \tag{2.1}$$

Quantum chromodynamics describes the interaction of the quarks and gluons, mediated by the strong force through color charge. Its Lagrangian has an $SU(3)_C$ color symmetry and is expressed as:

$$\mathcal{L}_{QCD} = -\frac{1}{4}\sum_i F^i_{\mu\nu}F^{i\mu\nu} + i\sum_r \overline{q}_{r\alpha}\gamma^\mu D^\alpha_{\mu\beta}q^\beta_r, \tag{2.2}$$

where q_r represent the quark field of flavor, α and β represent the color indices and $D^\alpha_{\mu\beta}$ is the covariant derivative, which is defined as:

$$D^\alpha_{\mu\beta} = \partial_\mu\delta^\alpha_\beta + \frac{i}{2}g_F\sum_i G^i_\mu\lambda^i_{\alpha\beta}, \tag{2.3}$$

where g_F is the strong coupling constant, λ_i are the matrices generators of SU(3) and the tensors $F^i_{\mu\nu}$ are defined as:

$$F^i_{\mu\nu} = \partial_\mu G^i_\nu - g_F f_{ijk}G^j_\mu G^k_\nu, \tag{2.4}$$

where G^i (i=1,..,8) represent the eight gluonic fields and f_{ijk} are the SU(3) structure constants.

The electroweak (EW) Lagrangian is invariant under gauge transformations of $SU(2)_L \times U(1)_Y$, where $SU(2)_L$ refers to the weak isospin I and $U(1)_Y$ to the weak hypercharge Y. The $SU(2)_L$ group has three generators which give rise to three gauge vector boson fields. The corresponding gauge coupling is denoted as g_2. However, the EW theory physical observable gauge fields are the photon fields A_μ, the neutral Z boson field and the two charged W boson fields $W^\pm_\mu$, which is a linear superposition of the four gauge field of $SU(2)_L \times U(1)_Y$ gauge group

$$A_\mu = sin\theta_W W^3_\mu + cos\theta_W B_\mu, \tag{2.5}$$

$$Z_\mu = cos\theta_W W^3_\mu - sin\theta_W B_\mu, \tag{2.6}$$

$$W^\pm_\mu = \frac{1}{\sqrt{2}(W^1_\mu \mp iW^2_\mu)}, \tag{2.7}$$

where θ_W is the weak mixing angle, which is defined as:

$$tan\theta_W = \frac{g_1}{g_2}. \tag{2.8}$$

From Eqs. 2.5,2.6, 2.7 an invariant quantum field theory rise, with Lagrangian

$$\mathcal{L}_{EW} = i\sum_f \overline{f} d_\mu \gamma^\mu f - \frac{1}{4}\sum_G F^{\mu\nu}_G F_{G\mu\nu}, \tag{2.9}$$

where the sums are extended over all the fermionic fields f and the vector field G respectively, and the covariant derivative (D_μ) is defined as:

$$D_\mu = \partial_\mu - ig_G(\lambda^\alpha G_\alpha)_\mu, \tag{2.10}$$

where g_G is the coupling constant of a fermion to the field G_α and λ^α are the generators of the symmetry group G.

2.1.1 The Higgs mechanism

The Lagrangian symmetry structure does not permit the gauge bosons and the chiral fermions to have mass, so it is necessary to break the symmetry of the Lagrangian in order that the SM particles can acquire masses.

To break the $SU(2)_L \times U(1)_Y$ symmetry an isospin doublet is introduced:

$$\phi = \begin{pmatrix} \phi^\dagger \\ \phi^0 \end{pmatrix} = \frac{1}{\sqrt{2}} \begin{pmatrix} \phi_1 + i\phi_2 \\ \phi_3 + i\phi_4 \end{pmatrix}. \tag{2.11}$$

It only adds $SU(2)_L \times U(1)_Y$ multiplets in order that the Lagrangian retains all its symmetries. We add a left-handed doublet with weak isospin $\frac{1}{2}$, and the electric charge of the doublet are chosen to ensure that the weak hypercharge Y=+1. [8]

Then, a potential $V(\phi)$ is added for the field that will break the symmetry, the potential is given by:

$$V(\phi) = \mu^2(\phi^\dagger\phi) + \lambda(\phi^\dagger\phi)^2, \quad \text{with} \quad \mu^2 < 0 \tag{2.12}$$

This potential depends on two parameters: μ and λ, where $\lambda > 0$ is requested to ensure the existence of a lower bound for the potential, and $\mu^2 > 0$ so the symmetry of the $V(\phi)$ potential can be broken. On the other hand, the Lagrangian for the auto-interacting scalar field is:

$$L_{scalar} = (D^\mu\phi)^\dagger(D_\mu\phi) - V(\phi), \tag{2.13}$$

where D_μ is the covariant derivative associated to $SU(2)_L \times U(1)_Y$:

$$D_\mu = \partial_\mu + ig\frac{1}{2}\overrightarrow{\tau} \cdot \overrightarrow{W_\mu} + ig\prime\frac{1}{2}YB_\mu \tag{2.14}$$

where g and $g\prime$ are the coupling constants of the fermions to the W_μ for the SU(2) group. This field describes the charged W bosons, while the B_μ field is SU(1) group.

If $\mu^2 < 0$ the symmetry of the potential $V(\phi)$ may be broken because it has a minimal asymmetrical value:

$$\phi^\dagger\phi = -\frac{\mu^2}{2\lambda}, \tag{2.15}$$

so the vacuum expectation value of the field is $\phi_0 = \frac{v}{\sqrt{2}}$. A representation of a potential symmetry breaking is shown in Fig. 2.2.

When the symmetry $SU(2) \times U(1)$ is broken, the ground state of the electric charge symmetry group U(1) has:

$$Q = I_3 + \frac{Y}{2}. \tag{2.16}$$

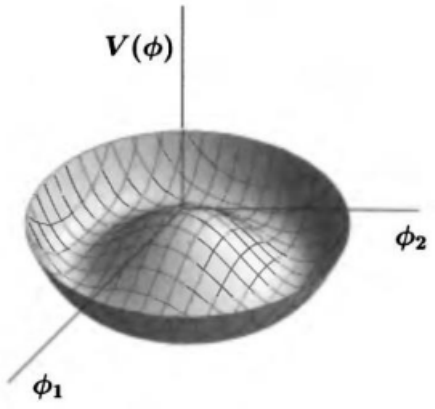

FIGURE 2.2: Potential of the Higgs field for $\mu^2 < 0$ [9]

In this case we choose $I = \frac{1}{2}, I_3 = -\frac{1}{2}$ and Y=+1, because this breaks $SU(2) \times U(1)$, but leaves $U(1)_{EM}$ invariant, leaving only the photon massless, so that the electric charge, weak isospin and the hypercharge are related. The field ϕ can be written as:

$$\phi = \frac{1}{\sqrt{2}} \begin{pmatrix} 0 \\ v + h^0 \end{pmatrix}.$$

The interaction of the Higgs field with the particles field generates their masses. If we expand $SU(2)_L \times SU(1)_Y$ around the ground state, we obtain:

$$g^2 W_\mu^i (W^j)^\mu \left[\phi \frac{\tau_i \tau_j}{4} \phi\right] - (g\prime)^2 \frac{1}{4} \frac{v}{2} B_\mu B^\mu + 2 g g\prime W_\mu^3 B^\mu \left[\phi \frac{\tau_3}{4} \phi\right] \tag{2.17}$$

From Eq. 2.17 we can extract the mass terms for each vectorial field in form of a matrix, given by:

$$\mathbf{M} = \frac{1}{4} v^2 \begin{pmatrix} g^2 & -g g\prime \\ -g g\prime & (g\prime)^2 \end{pmatrix} \tag{2.18}$$

For non-zero eigenvalues, the $W^\pm$ and Z bosonic fields acquire mass:

$$m_W = \frac{v}{2} g, \tag{2.19}$$

$$m_Z = \frac{v}{2} \sqrt{g^2 + g\prime^2}. \tag{2.20}$$

Differently from the Z boson, the γ boson remains massless, while the mass for the Higgs boson is given by:

$$m_h = \sqrt{2 \lambda v^2}. \tag{2.21}$$

The Higgs boson was discovered on July 2012, by the ATLAS and CMS experiments [10] [11] which observed a new particle in the mass region around 126 GeV, consistent with the properties of the Higgs boson. On March 2013, the two experiments, with twice the data that was available in July 2012, found that the new particle resembled the Higgs boson even more.

2.1.2 Problems of the standard model

Despite of the great success of the SM, where many of its predictions have been confirmed experimentally to great accuracy, including the existence of the Higgs boson, it is clear that the SM cannot be the final theory to describe particle physics because it suffers from important problems that we describe below.

Gravity and neutrinos mass. The gravitational interaction is not fundamentally linked to the other interactions. This model does not explain why gravity is weaker than the nuclear and electromagnetic force. On the other hand, in the SM model the neutrinos do not have mass, but according to the neutrino oscillation experiments the neutrinos do have mass [2].

Dark matter. The Wilkinson Microwave Anisotropy Probe (WMAP) [12] is a spacecraft that measure the temperature differences that are observed in the cosmic microwave background (CMB), and is also able to measure the density and composition of the universe. WMAP measures the relative density of the baryonic and non-baryonic matter, and determines some properties of the non-baryonic matter and the interactions with the baryonic matter and with itself. WMAP discovered that the universe was flat and that the dark matter made up only 24% of the density required to produce a flat universe. In order to explain the flatness of the universe 71.4% of the energy density in the universe is dark energy, which has a gravitationally repulsive effect. Based on these and other measurements, it appears that the matter of the universe is composed by (Fig. 2.3):

- 4.9% of atoms.
- $\sim$ 27% of "dark matter". It is likely to be composed by sub-atomic particles that interact weakly with ordinary matter. Dark matter was proposed in 1933 by Friz Zwicky when he was studying the gravitational effects of the rotation speed of a cluster of galaxies. The particles of dark matter are involved in the gravitational and weak interaction, and must have a mass large enough to form dark matter [13]. In the SM there are no particles that satisfy these conditions.

- $\sim$ 68% of "dark energy". Measurements of the Cosmic Microwave Background (CMB) and analysis of a supernova of type Ia with a large redshift suggested that most of the energy content of the universe is of an undetermined form called dark energy.

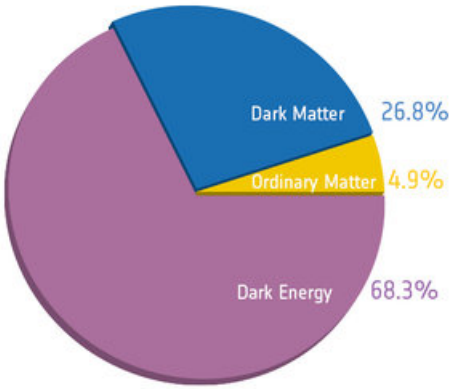

FIGURE 2.3: Composition of matter in the universe [14]

In the SM there are no particles that can be associated to dark matter, so it is necessary to propose new theoretical models.

Hierarchy problem. The hierarchy problem emerges from the radiative corrections of the mass of the Higgs boson. The major contribution to the Higgs boson mass is the one associated to the loop involving the top quark because the top quark is the particle with the greatest mass in the SM and hence the strongest Yukawa coupling to the Higgs boson. This loop introduces a quadratic divergence at high energies as shown in Fig. 2.4.

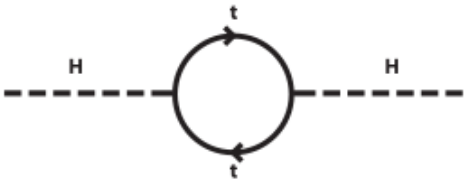

FIGURE 2.4: Loop of top quarks.[15]

The renormalized mass of the Higgs boson is given by:

$$m_H^2 = (m_H^0)^2 + \frac{3\Lambda^2}{8\pi_2 v_2}(m_H^2 + m_W^2 + m_Z^2 - 4m_t^2), \tag{2.22}$$

where m_H^0 is the bare mass of the Higgs boson, m_Z is the mass of the Z boson, m_W is the mass of the W boson, m_t is the mass of the top quark and Λ is the scale of adjustment. In order to disregard the term of the top quark and the W and Z boson, the mass of the Higgs boson must be adjusted in such a way that:

$$m_H^2 = 4m_t^2 - 2m_W^2 - m_Z^2 \approx (320\ GeV)^2. \tag{2.23}$$

2.2 Standard Model Effective Field Theory (SMEFT)

Since the SM theory is incomplete there has been a long search for BSM physics. So far there is no clear evidence for it, which motivates the use of an effective field theory (EFT) to characterise corrections to the Lagrangian of the SM.

BSM physics can be associated to the production of new particles. If a new particle exists with a mass below the energy reach of the LHC, it would appear as a peak in the spectrum of the invariant mass, as if there is a new particle with low mass we expect the presence of a bump at a certain point, as shown in Fig. 2.5 by the red line. If the mass is instead greater than the energy reached by the LHC the bump will not be seen, but the effect of this peak can still be seen as an increase in the tail of the SM distribution, as shown in Fig. 2.5 by the green line.

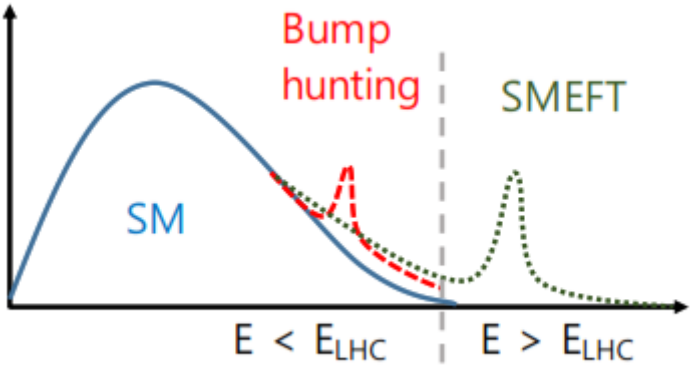

FIGURE 2.5: Schematic of new physics search within the energy range (red) of the LHC and beyond (green).

If a particle Ω has a mass Λ, there will be a new physical coupling $g^\star$, where its propagator is:

$$\frac{g_*^2}{p^2 - \Lambda^2.} \tag{2.24}$$

In the case that the particle mass is greater than the momentum of the interaction the propagator, Eq.2.24, then can be approximated as:

$$\frac{-g_*^2}{\Lambda^2}. \tag{2.25}$$

This means that the interaction with a massive mediator can be replaced by a point-like interaction, as shown in the Feynman diagrams in Fig. 2.6

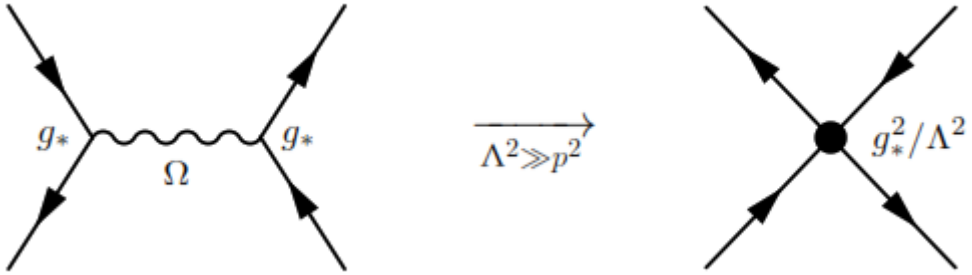

FIGURE 2.6: Feynamn diagram of a new particle Ω with mass Λ, that couples with the SM particle with a new coupling $g^\star$ (left), and the EFT vertex that describe the point-like interaction (right) [16].

We know that the SM Lagrangian is of dimension four, which means that all their operators are of dimension four and are scaled with a dimensionless coupling constant. To construct the SMEFT framework the SM Lagrangian is extended to higher order operators, which are combinations of the SM fields. This new Lagrangian is composed by a series of expansion in the inverse of the energy scale $1/\Lambda$, which is suppressed by powers of an energy scale Λ. The EFT Lagrangian is thus:

$$\mathcal{L}_{EFT} = \mathcal{L}_{SM} + \sum_{d>4} \sum_i \frac{C_i}{\Lambda^{d-4}} O_i^{(d)}, \tag{2.26}$$

where the index d represent the dimension of the operator O, the index i runs over all the operators of a given dimension, and C_i is a dimensionless coupling constant called Wilson coefficient. This coefficient parameterizes the strength of the new physics interaction. In this case we use dimension-six operators [17], and the number of operators depends on the flavour assumption. Assuming baryon B and lepton L number conservation, yields 59 dimension-six operators.

In order to search for new physics we measure the production cross-section, which can be expressed as the SM value plus an additional contribution due to the effects of the SMEFT. Using dimension-six operator, the cross-section becomes:

$$\sigma = \sigma_{SM} + \sum_i \frac{C_i}{\Lambda^2} \tilde{\sigma}_i + \sum_{ij} \frac{C_i C_j}{\Lambda^4} \tilde{\tilde{\delta}}_{ij}, \tag{2.27}$$

where i and j run over all the operators. The term $\tilde{\sigma}_i$ represent the strength of interference of the SMEFT operator with SM, while $\tilde{\delta}_{ij}$ represent the pure EFT contribution.

Since no signs of new particles have been found at the LHC, new particles may emerge in the TeV region. For this we need to use lower limits on Λ to constrain its form. Baryon number, lepton number and CP can be approximated symmetries of the new theory at the TeV scale. A solution to this is to impose that the EFT respect the Minimal Flavour Violation (MFV). MFV requires that all flavour and CP violations are related to the Yukawa coupling. Under the assumption of MFV the dimension-six operators can be divided into the ones that involved four heavy quarks (4H) and those who involve two heavy and two light quarks (2H2L). In tables 2.1 and 2.2 we show the operators based on the basis used by the LHC Top Working Group [18].

4H
c^1_{QQ}
c^8_{QQ}
c^1_{Qt}
c^8_{Qt}
c^1_{Qb}
c^8_{Qb}
c^1_{tt}
c^1_{tb}
c^8_{tb}
c^{1I}_{QtQb}
c^{8I}_{QtQb}

TABLE 2.1: Dimension six-operators for the flavour B, L conserving degrees of freedom for four heavy quarks [18]

2H2L
$c^{3,1}_{Qq}$
$c^{3,8}_{Qq}$
$c^{1,1}_{Qq}$
$c^{1,8}_{Qq}$
c^1_{Qu}
c^8_{Qu}
c^1_{Qd}
c^8_{Qd}
c^1_{tq}
c^8_{tq}
c^1_{tu}
c^1_{td}
c^8_{td}

TABLE 2.2: Dimension six-operators for the flavour B, L conserving degrees of freedom for two heavy quarks and two light quarks [18].

Chapter 3

Experimental framework

3.1 Fundamental Concepts

3.1.1 Cross-section

For the calculation of an inclusive cross-section in a proton-proton collision we have to consider the parton distribution functions (PDFs) and the combination of different initial partons. The cross-section σ for a hard scattering with two hadrons in the initial state can be defined as

$$\sigma(P_1, P_2) = \sum_{i,j} \int dx_1 dx_2 f_i(x_1, \mu_F^2) f_j(x_2, \mu_F^2) \hat{\sigma}_{i,j}(p_1, p_2, Q^2/\mu_F^2, Q^2/\mu_R^2), \tag{3.1}$$

where P_1 and P_2 are the four-momenta of the initial hadron and p_1 and p_2 are the four momenta of the partons present in the hard interactions. The parameters x_1 and x_2 are the fractions of momentum carried by the partons, f_i and f_j are the PDFs for the partons at a factorization scale μ_F. Q^2 is the characterization scale of the scattering, and μ_R is the renormalization scale. Partons carry only a fraction of the four momentum of the initial proton, which gives a parton level center-of-mass energy $\sqrt{\hat{s}}$ smaller than the total proton-proton energy $\sqrt{s}$. Both of them can be related by a factor τ, which is defined as:

$$\tau = x_1 x_2 = \frac{\hat{s}}{s}, \tag{3.2}$$

where $\hat{s} = (p_1 + p_2)^2$ and $s = (P_1 + P_2)^2$. The differential parton luminosity is defined as:

$$\frac{dL_{i,j}}{d\tau} = \frac{1}{\tau} \frac{1}{(1 + \delta_{i,j})} \int dx_1 dx_2 [x_1 f_i(x_1) x_2 f_j(x_2) + (1 \to 2)] \delta(\tau - x_1 x_2), \tag{3.3}$$

so the cross section is given by:

$$\sigma(s) = \sum_{i,j} \int \frac{d\tau}{\tau} \left(\frac{1}{s} \frac{dL_{i,j}}{d\tau} \right) \hat{s}\hat{\sigma}_{i,j}. \tag{3.4}$$

3.1.2 Luminosity

In scattering theory the instantaneous luminosity is defined as the ratio of the number of events in a certain time interval (dt) to the cross section(σ):

$$\mathcal{L} = \frac{1}{\sigma} \frac{dN}{dt}. \tag{3.5}$$

The instantaneous luminosity is determined by the overlap of the core of the beam distribution. To calculate the instantaneous luminosity, we assume Gaussian profiles in all dimensions of the form:

$$\rho_{iz}(z) = \frac{1}{\sigma_z \sqrt{2\pi}} exp\left(-\frac{z^2}{2\sigma_z^2} \right) \quad \text{where} \quad i = 1, 2, \quad z = x, y. \tag{3.6}$$

We assume equal beams, which means that $\sigma_{1x} = \sigma_{2x}$, and $\sigma_{1y} = \sigma_{2y}$. The instantaneous luminosity is given by:

$$\mathcal{L} = \frac{N_1 N_2 f N_b}{4\pi \sigma_x \sigma_y}. \tag{3.7}$$

Where N_1 and N_2 are the number of protons in each bunch, N_b the number of bunches and f the revolution frequency

The integrated luminosity is defined as:

$$L = \int \mathcal{L} dt. \tag{3.8}$$

The integrated luminosity collected by the CMS experiment for proton-proton collision at $\sqrt{s} = 13$ TeV is shown in Fig. 3.1

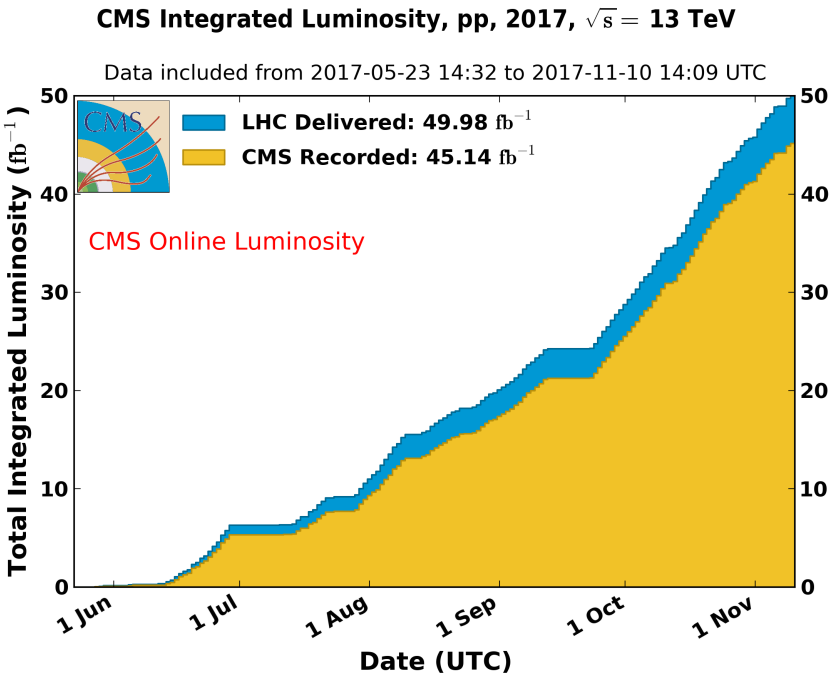

FIGURE 3.1: Cumulative integrated luminosity of the CMS experiment in 2017 [19]

3.2 Jets

Quarks, gluons and antiquarks are the constituents of protons, neutrons and other hadrons, but they are never observed isolated by themselves. A high energy quark is transformed into a spray of hadrons, called jets. The hadronic final states appear as a collection of particles, called jet of hadrons. In Fig. 3.2 is shown the relation between the parton level of outgoing particles and the hadronic final state.

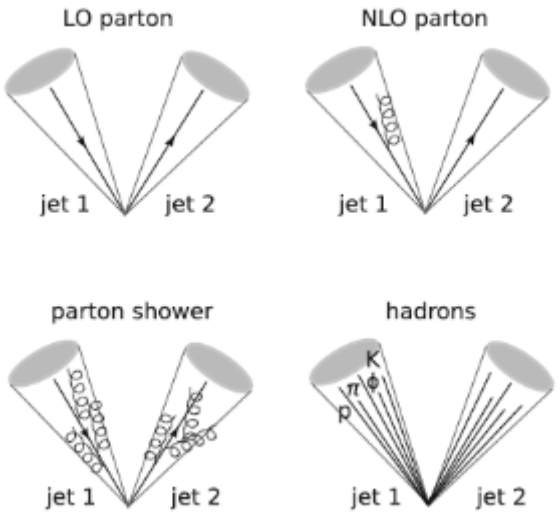

FIGURE 3.2: Illustration of the evolution from the partonic final state to the hadronic final state [20]

Jets are measured and studied in order to determine the properties of the original quarks. There exist different techniques to identify jets, that we explain below:

3.2.1 Cone algorithm

First, particles are classified according to their transverse momentum (p_T). The particle with the highest p_T is defined as the central particle. The algorithm looks for particles inside a cone of fixed radius ΔR around the central particle, in terms of the pseudo-rapidity η and the azimuthal angle ϕ of the central particle (denoted by c) and the i-th particle, defined as:

$$\Delta R_{ci} = \sqrt{(\Delta\eta)^2 + (\Delta\phi)^2}, \tag{3.9}$$

where $\Delta\eta = \eta_c - \eta_i$ and $\Delta\phi = \phi_c - \phi_i$. Then the algorithm determines the total momentum of the particles that are inside the cone, i.e. $\Delta R_{ci} < \Delta R$, associating this value to the central particle of the next iteration. If the momentum is the same as the momentum of the central particle, a stable cone is defined as a jet and all the particles inside the cone are removed. The interaction stops when all particles in an event are inside a specific jet.

3.2.2 Sequential clustering algorithm

This algorithm assumes that particles within jets have small differences in transverse momenta. The first distance variable is between two particles i and j:

$$d_{ij} = min(p_{ti}^a, p_{tj}^a) \times \frac{R_{ij}^2}{R}, \tag{3.10}$$

where R is the radius parameter which determines the final size of the jet, and R_{ij}^2 is the $(\eta - \phi)$ space distance between the two particles, defined as

$$R_{ij}^2 = (\eta_i - \eta_j)^2 + (\phi_i - \phi_j)^2 \tag{3.11}$$

The second distance variable is $d_{iB} = p_{ti}^a$, the momentum space distance between the beam axis and the detected particle. This algorithm first find the minimum of the entire set d_{ij}, d_{iB} [21]. Based in the value of the parameters a, two specific algorithms are defined as follows: for $a = 2$. In this case the definitions are:

- k_t algorithm

$$d_{ij} = min\left(p_{ti}^2, p_{tj}^2 \times \frac{R_{ij}^2}{R}\right) \tag{3.12}$$

$$d_{iB} = p_{ti}^2 \tag{3.13}$$

  The k_t algorithm prefers to cluster soft particles first.

- Anti-k_t algorithm for $a = -2$ and corresponding to:

$$d_{ij} = min\left(\frac{1}{p_{ti}^2}, \frac{1}{p_{tj}^2}\right) \times \frac{R_{ij}^2}{R} \tag{3.14}$$

$$d_{iB} = \frac{1}{p_{ti}^2} \tag{3.15}$$

  This algorithm prefers to cluster hard particles first. The anti-k_t algorithm generates a circular hard jet, which clips a lens-shaped region out of the soft one. In Fig. 3.3 is shown an event with several jets reconstructed using this algorithm with R=1.

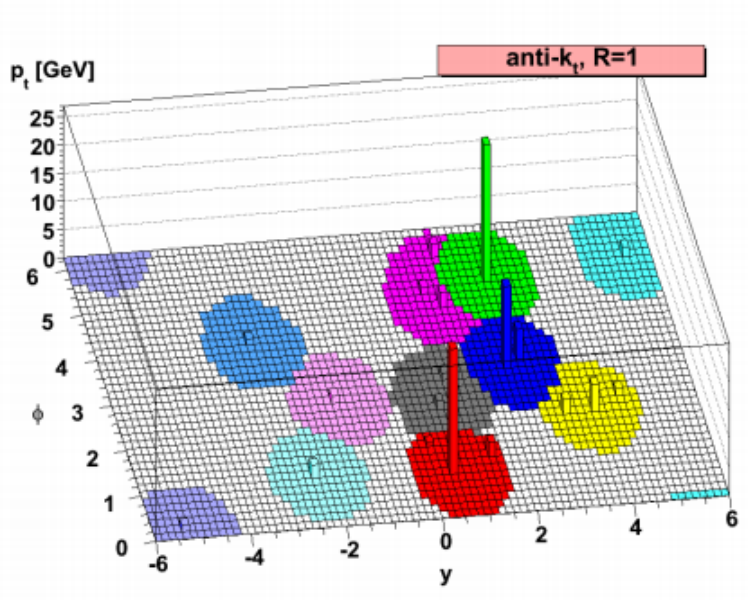

FIGURE 3.3: An example of events containing several jets reconstructed with the anti-k_t algorithm [22].

3.3 Large Hadron Collider (LHC)

The LHC is the world's largest and powerful particle accelerator. It consists of a 27 kilometer ring of superconducting magnets with a number of accelerating structures to boost the energy of the particles along the way. The accelerator tubes and collision caverns are 100 meter underground. Inside the accelerator, there are two high-energy proton beams accelerated by radio frequency (RF) cavities, up to a speed close to the speed of light. The beams travel in opposite directions in separate beam pipes and they are guided around the accelerator ring by a strong magnetic field maintained by superconducting electromagnets. The collider operates typically with more than 2808 bunches per beam. The collisions create the conditions to produce many elementary particles.

To reach the colliding energy the proton beams go through different acceleration steps. These steps are shown schematically in Fig. 3.4.

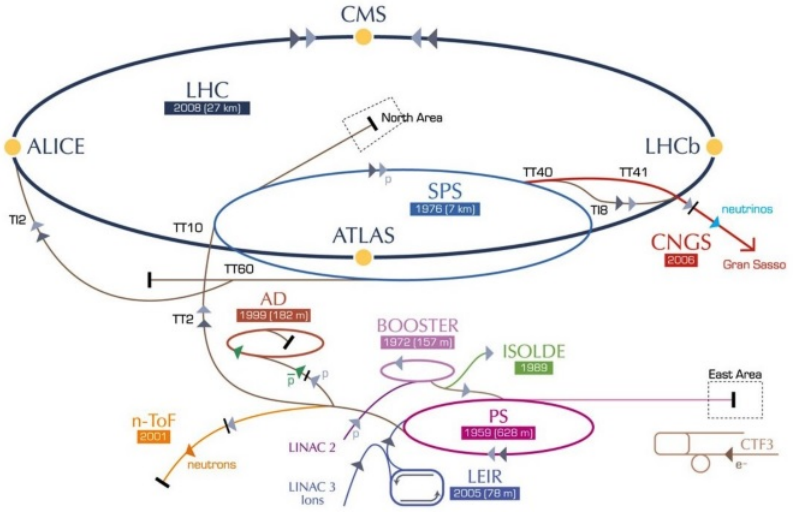

FIGURE 3.4: schematic of the acceleration process [23].

First, protons are produced in the LINAC and then they are accelerated in the booster. After that they are delivered to the proton synchrotrons where they acquire an energy of 450 GeV. Finally, they pass to the main ring to achieve their final energy and then they collide in one of the four main detectors: The Compact Muon Solenoid (CMS), the Toroidal LHC Apparatus (ATLAS), the LHCb or the Large Ion Collider Experiment (ALICE). The ATLAS detector has an inner tracker that detects and analyzes the momentum of the particles and calorimeters surrounding the inner tracker to measure the particles energy. This detector also has a muon spectrometer to measure the momentum of each muon. The ALICE experiment is used to study collisions between heavy ions, and with these collisions scientist expect to see the ions breaks apart into a mixture of a quark and a gluon. The main purpose of the LHCb is to investigate the difference between matter and anti-matter through the study of b quarks.

3.3.1 CMS experiment

The CMS detector is 21.6 m long and has a diameter of 14.6 m . The central feature of the CMS apparatus is a superconducting solenoid of 6 m internal diameter. The solenoid magnet is located at the center of the CMS detector, it has a length of 12.9 m that cover the barrel region of the detector. The solenoid is composed by 2168 turns of superconducting niobium-titanium, and runs a current of 19.5 kA at a temperature of 4.6 K. Inside the solenoid there is an homogeneous magnetic field of 3.8 T. The coordinate system used in the CMS detector has the origin at the collision point, the y-axis point towards the surface, the x-axis towards the center of the accelerator ring, and the z-axis points along the beam axis. The pseudorapidity is used instead of polar angles since it

is Lorentz invariant, this is given by:

$$\eta = -ln\left[tan\frac{\theta}{2}\right]. \tag{3.16}$$

The tracking system measures the trajectories of charged particles. It covers an azimuth angle (ϕ) from 0 to 2π, allowing the measurement of momentum balance in the plane transverse to the beam direction, and it covers a pseudorapidity range $|\eta| < 2.5$. The tracking system consist of large silicon strips and an innermost silicon pixel detector, so it can maintain a good signal-to-noise ratio. For single muons with high momentum tracks the resolution is about 1 to 2%, the transverse impact parameter resolution is about 10 μm, while a low momentum track is degraded by multiple scattering. For pions and hadrons the efficiency is lower due to the interaction with the materials in the tracker. A part of the tracking system is the pixel system, which is responsible for measuring small impact parameters. It contributes also tracking points in $r - \phi$ and z, and is very important to the reconstruction of secondary vertices from b and tau decays. A lead-tungstate crystal electromagnetic calorimeter and a brass and scintillator hadron calorimeter surround the tracking volume, and provide energy measurements of electrons, photons and hadronic jet in the range of $|\eta| < 3.0$, while muons are measured within $|\eta| < 2.4$ by gas ionization detectors embedded in the steel flux-return yoke of the solenoid [24].

The electromagnetic calorimeter (ECAL) is hermetic; it measures the energy of emerging particles, in particular of electrons and photons. It is made with lead tungstate ($PbWo_4$) scintillator crystals, having a high density of 8.28 g/cm^3, a radiation length of 0.89 cm and a Moliere radius of 2.2 cm. Because of the crystal characteristic this is a fine granularity and compact calorimeter. When electromagnetic showers pass through the crystals they generate light which is then capture in photodiodes with intrinsic gain in order to amplify the signal. The ECAL detector is composed by three parts: the barrel ECAL (EB), the endcap ECAL (EE) and the ECAL preshower (ES), which is placed in front of the endcap crystal.

The EB is made of 61200 crystals, it has a granularity of 360-fold in ϕ and 2×85-fold in η, covering the pseudorapidity range $|\eta| < 1.479$. The cross-section of the crystal is 0.0174×0.0174 in $\eta - \phi$. Moreover, the EE is composed by 7324 crystals in each of the two endcaps. It cover a pseudorapidity range $1.479 < |\eta| < 3.0$, and consists of identical crystals grouped in units of 5×5 crystals consisting of a carbon-fibre alveola structure. Finally, the preshower detector is composed by two layers of lead absorbers, with silicon strips behind them. This detector helps to identify the neutral pions in the endcaps, and the position of the electrons and photons with high granularity, in the

region $1.653 < |\eta| < 2.6$. A schematic overview of the ECAL detector is shown in Fig. 3.5.

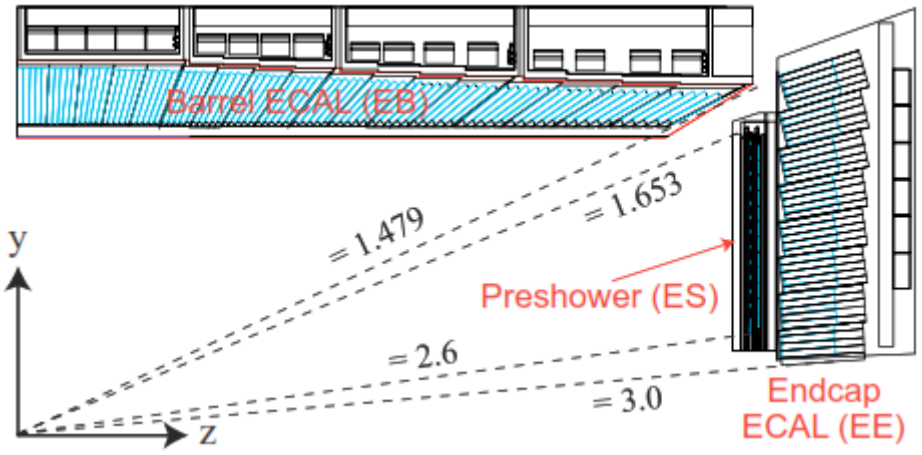

FIGURE 3.5: Schematic of the electromagnetic calorimeter system [25]

The hadron calorimeter (HCAL) is placed after the ECAL calorimeter and it measures the hadron jets, providing indirect measurement of neutrinos and exotic particles that do not interact. The calorimeter finds the position, energy and arrival time of the particle. In order to measure the particle energy, the calorimeter use alternating layers of absorber and fluorescent scintillator, which produce a light pulse when the particle passes through, then special optic fibers collect the produced light and feed it into readout boxes where photodetectors amplify the signal. It is organized into barrel, the HB and HO, an endcap (HE) and forward (HF) sections. The (HB) consist of 36 identical azimuthal wedges [24]. This system cover a pseudorapidity range of $|\eta| < 1.4$. The HO system has an additional layers of scintillators outside the magnet volume. In this system the remaining parts of the hadronic shower are captured, increasing the resolution on the missing transverse energy and the energy of the jets. The HB/HO system covers a range of $|\eta| < 1.26$. On the other hand the HE system have 2304 modules with a much broader segmentation but with the same pseudorapidity segmentation as the HB, covering a range of $1.3 < |\eta| < 3.0$. Finally, we have the HF, which is located close to the beampipe and covers a range of $3.0 < |\eta| < 5.2$. It is made of steel absorbers with quartz scintillating fibre. This system is based on Cherenkov light produced in the quartz fibres. The energy resolution for the hadronic calorimeter is of the order of 10-20% for hadrons with an energy between 50 and 100 GeV. The schematic of the hadronic calorimeter is shown if Fig. 3.6.

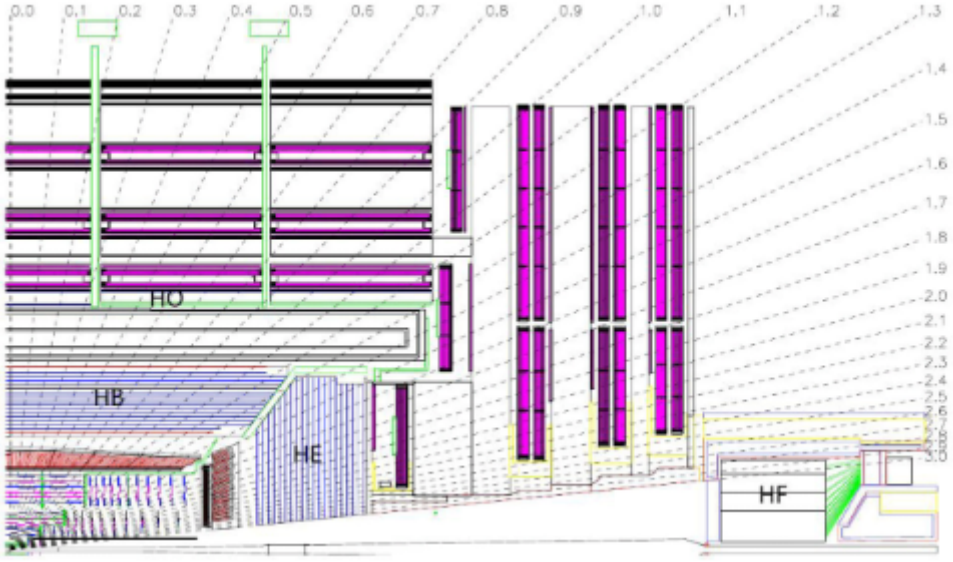

FIGURE 3.6: Schematic representation of the hadronic calorimeter [25].

The muon system has 3 functions: muon identification, measurement of the momentum, and triggering. The system reconstructs the momentum and charge of the muon over all the kinematic range of the LHC. It has a cylindrical, barrel section and 2 planar endcap regions. The barrel drift tube chambers cover the pseudorapidity region $|\eta| < 1.2$ and are organized into 4 stations. The first 3 stations contain 8 chambers, in 2 groups of 4, which measure the muon coordinate in the $r-\phi$ bending plane, and 4 chambers measure in the z direction [26].The drift tubes allow for an excellent spatial resolution. In the second endcap region the muon system uses cathode strip chambers (CSC), which are multi-wired proportional chambers composed by anode wires that are oriented parallel to the cathode in a gaseous volume. The signals from the anode wires are fast and can be used in the trigger. The CSC identify muons that have $|\eta|$ values between 0.9 and 2.4. Because the muon detector covers the full pseudorapidity interval $|\eta| < 2.4$ with no acceptance gaps, the muons identification is in the range $10° < \theta < 170°$. Each of these modules are supplemented with a resistive plate chamber (RPC) allowing a precise timing resolution of the order of 1 ns. The first level of the CMS trigger system, uses the information from the calorimeters and the muon detectors to select the most interesting events in a fixed time interval of less than $4\mu s$. A diagram of the detector is shown in Fig. 3.7.

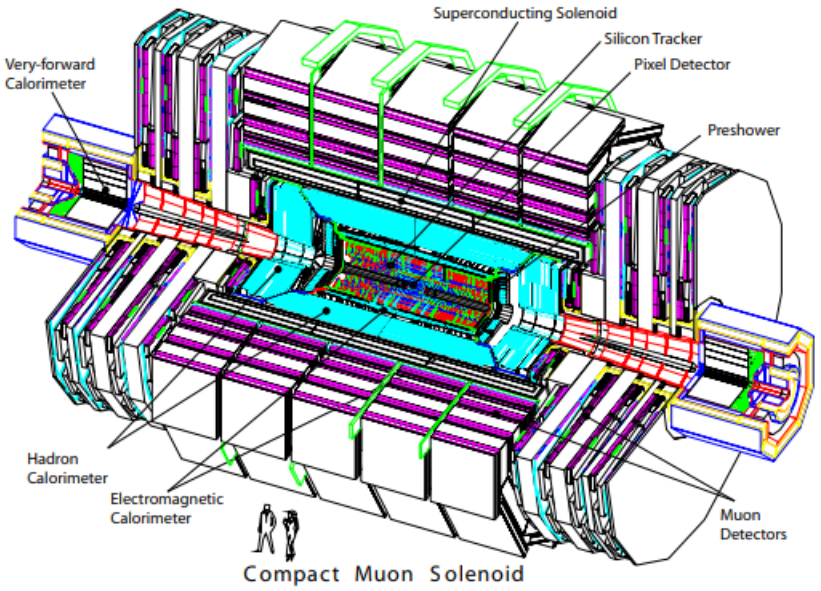

FIGURE 3.7: A perspective view of the CMS detector [26].

Chapter 4

Top quark physics

4.1 Production of Top quarks at LHC

Particles at the LHC are produced by proton-proton collisions. Classically, the proton is composed by two up quarks and one down quark, but in a quantum mechanical description there is a probability that all quarks and gluons are present in the protons, this probability being described by the proton parton density function (PDFs). These PDFs are functions of the fractional momentum of the proton that the parton carries.

At the LHC top quarks are produced singly, in pairs, and also four of them at the same time by proton-proton collisions, where each process has its own cross section and final states. The top quark pair production is the one with higher cross-section. This final state is produced in two different ways: the first one is by gluon fusion, as illustrated by the leading order (LO) Feynman diagram in Fig. 4.1, the second one is by the annihilation of a quark and anti-quark, as shown in Fig. 4.2

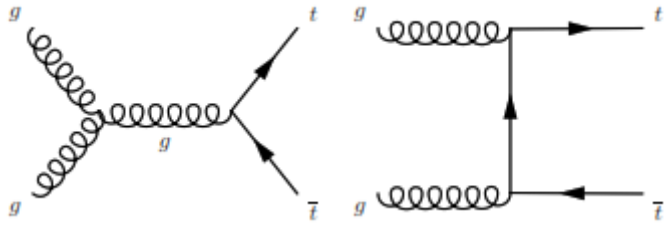

FIGURE 4.1: LO Feynman diagrams of the top quark pair production by gluon fusion at the LHC.

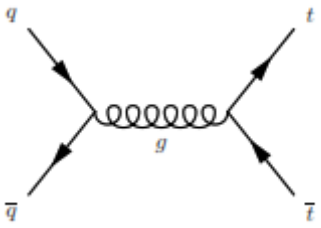

FIGURE 4.2: LO Feynman diagram of the top quark pair production by quark anti-quark annihilation at the LHC.

The theoretical calculation of the cross-section at the next-to-leading order (NLO) for the top quark pair production at a center-of-mass energy of 13 TeV amounts to $\sigma_{t\bar{t}} \approx 831$ pb [27].

On the other hand, the production of a single top quark can occur in three ways: the s-channel, t-channel and the tW production. The Feynman diagrams of these process are shown in Fig. 4.3. These diagrams involve mostly electroweak processes.

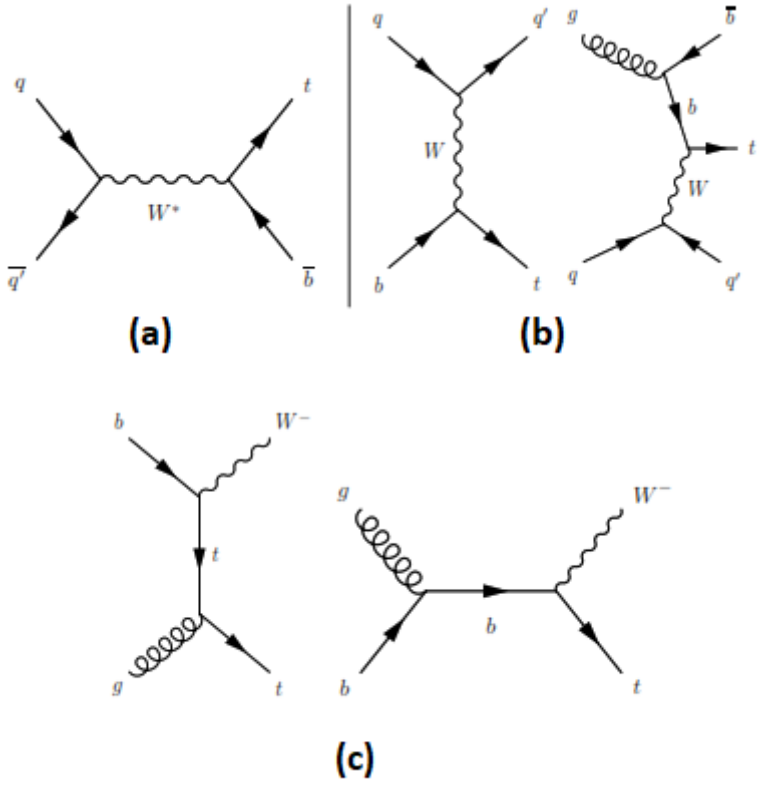

FIGURE 4.3: LO Feynman diagrams of: (a) the s-channel, (b) t-channel and (c) the tW production.

The cross section for each of these process are shown in Table 4.1

Process	cross-section
s-channel	10.32 pb
t-channel	216.99 pb
tW production	71.7 pb

TABLE 4.1: Cross-section for different processes of single top quark production.

Another way in which top quarks are originated is by producing 4 quarks at the same time, although this process has a very low cross-section of about 9.2 fb. This is a very rare process but it is interesting to study it since it has a great sensitivity to new physics effects.

4.2 Top quark decays

Most of the particles can decay by several different routes and in such circumstances the total decay rate is the sum of all individual decay rates

$$\Gamma_{tot} = \sum_{i=1}^{n} \Gamma_i, \tag{4.1}$$

The branching ratio is the fraction of all particles of the given type that decay by each mode. The branching ratios are determined by the decay rates as follow:

$$BR_i = \Gamma_i / \Gamma_{tot}. \tag{4.2}$$

Top quarks decay through electroweak interaction into a W boson and a bottom quark with a branching ratio near 100%. The different top quark decays are classified according to the decay of the W boson. The branching ratio of W decaying to quarks is 67% and the branching ratio of the W decaying to lepton-neutrino pairs is 33%. Given this, there are three possible decay channels to study for top quark pair production:

- All-hadronic channel: In this channel both W bosons decay to two quarks and originate two jets ($W^{\pm} \to jj$). This channel has a branching ratio of $\sim 45\%$. In this case in the final state there are 2 b-jets and 4 jets which come from the W decays (Fig. 4.4).

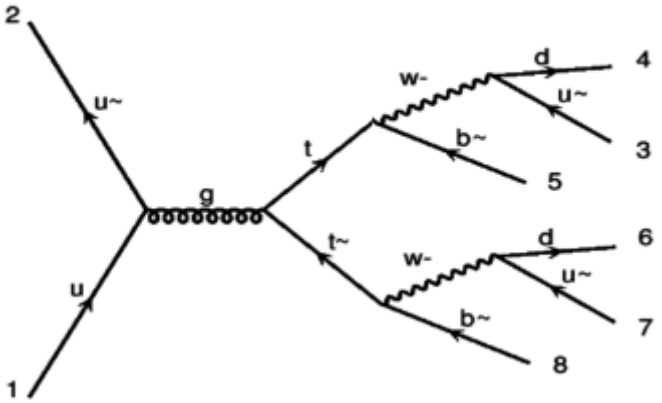

FIGURE 4.4: Diagram of the top quark decay in the all-hadronic channel

- Semi-leptonic channel: In this channel one W decays into two jets and the other to a lepton-neutrino pair, as

$$W^+ \to jj, W^- \to l\overline{\nu_l}, \tag{4.3}$$

or

$$W^+ \to l\overline{\nu_l}, W^- \to jj \tag{4.4}$$

This channel has a branching ratio of $\sim 45\%$. In the final state there are an undetected neutrino, one charged lepton, 2 b-jets, 2 jets and missing transverse energy that comes from the neutrino (Fig. 4.5).

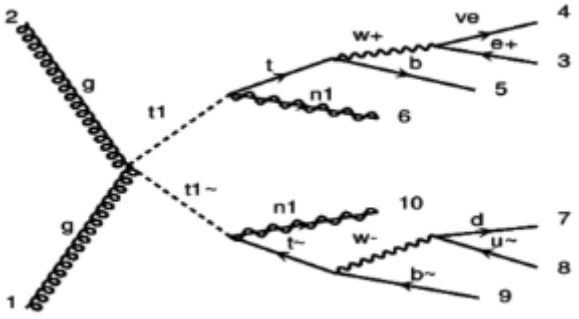

FIGURE 4.5: Diagram of the top quark decay in the semi-leptonic channel

- Dileptonic channel: Both W bosons decay into a lepton-neutrino pair, according to

$$pp \to tt \to W^+ b W^- \overline{b}, \tag{4.5}$$

where

$$W^+ \to \nu_l \bar{l}, \tag{4.6}$$

$$W^- \rightarrow \overline{\nu_l} l \tag{4.7}$$

This channel has a branching ratio of $\sim 10\%$

FIGURE 4.6: Diagram of the top quark decay in the dileptonic channel

In the final state there are two bjets, two undetected neutrinos and two charged leptons (see Fig. 4.6). So in this channel there is more missing transverse energy that comes from the two neutrinos. The BR value for the leptonic channel is reduced if only electrons and muons are considered as charged leptons

4.3 Effective Field Theory in CMS

There are four current approaches to use the Effective Field Theory in analyses at the CMS. The first one is based on the reinterpretation of an inclusive measurement, such as the cross-section of an SM process. In this case they use this quantity to constrain the Wilson coefficients by using EFT parametrizations. The second approach relies on the reinterpretation of differential measurements, where different quantities are measured that are sensitive to EFT at parton and particle level. The third approach considers hybrid EFT measurements at detector level. The last one characterizes EFT directly, comparing EFT simulations to the observed data.

4.3.1 Reinterpretation of an inclusive measurement

There are several analyses using this approach. One of these measures the cross-section of top quark pair production in association with a W or Z boson using proton-proton collision at a center-of-mass energy of 13 TeV with an integrated luminosity of 35.9 fb^{-1} [28]. These productions are among the most massive signatures that can be studied with high precision. The analysis is done for three final states:

- The production of $t\bar{t}W$ events decaying in 2 leptons with the same charge (SS). This channel has less backgrounds because other processes with same-charge leptons

have small cross-section. In this case, two SS leptons ($\mu\mu$, μe, ee) requiring the transverse momentum (p_T) of both leptons to be more than 25 GeV, and the electron with higher with higher p_T have $p_T > 40$ GeV are selected. In order to suppress the different backgrounds for this channel, the invariant mass of the two leptons is required to be greater than 12 GeV, and that the missing transverse energy (p_T^{miss}) greater than 30 GeV.

- The production rate of $t\bar{t}Z$ events is measured in the final state with three leptons. Events are selected to contain exactly three leptons ($\mu\mu\mu$, $\mu\mu e$, eee), requiring the leading, sub-leading and the trailing lepton p_T to be greater than 40, 20, and 10 GeV, respectively. To reduce the background the difference between the invariant mass of the lepton pair, $M(ll)$, and of the Z boson, $M(Z)$, be smaller than 10 GeV.

- The final state with four leptons is used to measure the signal of $t\bar{t}Z$. This channel is characterized by the presence of two b-jets, four leptons and large missing transverse energy. The leading jet must have $p_T > 40$ GeV, the invariant mass of any lepton pair has to be greater than 10 GeV, and $|M(ll) - M(Z)| < 20$ GeV. To distinguish the signal from the background a multivariate analysis (MVA) was used. The observables that were used to discriminate the signal are: number of jets, N_j, number of b-jets, N_b, the scalar sum of p_T of the jets, H_T, p_T^{miss}, the invariant mass of the lepton pair, M_T, the highest and lowest p_T of the jets, and the separation ΔR between the trailing lepton and the nearest selected jet.

In this research the final state with two leptons was used to extract the signal of $t\bar{t}W$ events and the state with three or four leptons to measure the signal of $t\bar{t}Z$. Using the cross-sections obtained from each process, the Wilson coefficient of eight dimension-six operators are constrained. These operators are of particular interest since they modify the expected cross-section of $t\bar{t}W$ and the $t\bar{t}Z$. $t\bar{t}Z$ is affected by $\mathcal{O}_{3G}$, $\mathcal{O}_{2G}$, $\mathcal{O}_{uB}$. Only $t\bar{t}Z$ is affected by $\mathcal{O}_{Hu}$, and all these process are affected by $\mathcal{O}_{uG}$ and $\mathcal{O}_{uW}$. The constrain presented in this analysis was obtained by considering one operator at a time.

The other research is for the the standard model production of four top quarks using single-lepton channel with exactly one muon or electron plus jets, and opposite-sign dilepton, ($\mu^+\mu^-$, $\mu^\pm e^\mp$, e^+e^-), plus jets ($pp \to t\bar{t}t\bar{t}$) [29]. For the single-lepton channel is required at least one isolated muon with $p_T > 24$ GeV and $|\eta| < 2.4$ or an isolated electron with $p_T > 32$ GeV and $|\eta| < 2.1$. For the dilepton channel they required $|\eta| < 2.4$ for muons and $|\eta| < 2.5$ for electrons. To identify the top quarks and improve the discrimination between signal and background boosted decision trees (BDTs) were

used. In this case only four operators contribute to $t\bar{t}t\bar{t}$ production: $\mathcal{O}^1_{tt}$, $\mathcal{O}^1_{QQ}$, $\mathcal{O}^1_{Qt}$, and $\mathcal{O}^8_{Qt}$.

4.3.2 Reinterpretation of differential measurements

One analysis uses this approach for the measurement of the differential cross-section of the top quark pair production containing two oppositely charged leptons. The differential cross-sections are presented as a function of the kinematic observables, and are defined with parton level quarks in a fiducial and full phase space. For each observable the absolute and normalized differential cross-sections are calculated. All the results are compared with standard model predictions from Monte Carlo simulations with next-to-leading-order (NLO). The absolute particle-level differential cross-section as a function of $\Delta\phi(ll)$ is used to constrain the top quark chromomagnetic dipole moment [30].

Another study has been carried measuring the top quark polarization and $t\bar{t}$ spin correlations using dilepton final states. The differential cross-section, sensitive to the independent coefficients of the spin dependent parts of the $t\bar{t}$ production density matrix is measured. The measured distribution is then compared with SM predictions using NLO accuracy in QCD. In this analysis the distributions are corrected to a parton level and extrapolated to the full phase space. A significant discrepancy with respect to the expectation of the SM was not found. In order to constrain the contributions from ten dimension-six effective operator statistical and systematic covariance matrices were used in simultaneous fits. Two of these operator represent the anomalous chromomagnetic, and chromoelectric dipole moments, and constraints on their Wilson coefficients of $-0.24 < C_{tG}/\Lambda^2 < 0.07\ TeV^{-2}$ and $-0.33 < C^t_{tG}/\Lambda^2 < 0.20\ TeV^{-2}$, were obtained at the 95% confidence level [31].

4.3.3 Hybrid EFT measurements at detector level

Top quark pair production in association with a Z boson has been studied for final states with three or four leptons. The measured inclusive cross-section $\sigma(t\bar{t}Z) = 0.95 \pm 0.06$ pb is in good agreement with the SM prediction of 0.84 ± 0.10 pb.The differential cross-section is measured as a function of $p_T(Z)$ and $cos\theta^*_Z$, and it is defined in the phase space where the top quark pair is produced in association with two leptons with an invariant mass of $70 < M(ll) < 110$ GeV. The cross-sections are then calculated from the measured event yield. For this analysis an anomalous coupling Lagrangian is considered, which contains neutral vector and axial-vector current couplings, written as

$$\mathcal{L} = e\overline{u}_t \left[\gamma^\mu(C_{1,V} + \gamma^5 C_{1,A}) + \frac{i\sigma^{\mu\nu}p_\nu}{m(Z)}(C_{2,V} + i\gamma_5 C_{2,A})\right] v_{\bar{t}} Z_\mu. \tag{4.8}$$

This study is based on the interpretation given in the context of SMEFT in the Warsaw basis formed by 59 independent Wilson coefficients, where only 15 are have a large impact in this process. They consider separately the operators that induce anomalous interactions of the top quark with the remaining neutral gauge bosons, the Z boson and the photon. For this case the relevant Wilson coefficients are c_{tZ}, $c_{tZ}^{[I]}$, $c_{\phi t}$, and $c_{\bar{\phi}Q}$ [32].

Another search of new physics is done using $t\bar{t}$ and tW events in dilepton final states. All dimension-six operators are investigated that contribute to top quark pair production and single top quark production in association with W boson. The EFT effect in the production of the top quarks and not in the decays are considered. The search is sensitive to new physics contributions to tW and $t\bar{t}$ production, and the six effective couplings, C_G, $C_{\phi q}^{(3)}$, C_{tW}, C_{tG}, C_{uG}, and C_{cG}, assuming one non-zero at a time, are constrained. A deviation from the SM prediction has been seen for C_G, $C_{\phi q}^{(3)}$, C_{tW}, C_{tG} [33].

Chapter 5

Methodology

5.1 Simulation programs

In the following, the possible presence of BSM physics will be characterized comparing events produced according to EFT models, to those expected instead from SM. To this purpose, proton-proton collision events are simulated using the MadGraph Monte Carlo generator followed by Pythia for the parton showering, to produce a description of the events at hadron level, which can be studied with the MadAnalysis package. This is followed by the Delphes program for the simulation of the CMS detector. An illustration of the two stages of stages of simulation is provided by the simple cartoon of Fig. 5.1

5.1.1 Madgraph

MadGraph [34] is a matrix-elements (ME) generator, and it is written in Python programming language. In a proton-proton collision at high energies, there is a probability that the particles generated in the collision have large momentum: this is considered a

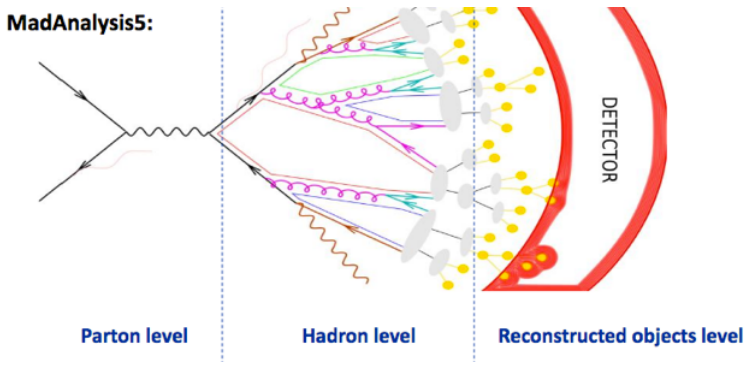

FIGURE 5.1: Illustration of the two stages of the simulation.

hard scattering and the calculations must be done using perturbative QCD. The two principal processes that MadGraph executes are: 1) the formulation of the Lagrangian for the study of processes from the standard model or from additional physics BSM; 2) a complete next-to-leading-order optimization of next to leading order (NLO) calculations for SM and BSM processes. The theory used for the computation has to be declared. As a result, MadGraph generates the Feynman diagrams and calculate the matrix-elements amplitudes at randomly chosen points of phase-space. These amplitudes are then used by MadEvents [34] to compute cross-sections for the chosen processes.

5.1.2 Pythia

Pythia [35] is used in the study of particle collisions at high energies where final multi-hadronic states are generated. In this program there is a great number of analytic models based on QCD, that can cover several phenomena at subatomic scale, such as initial/final states parton shower, decays, hard and soft interactions, parton distribution, hadronization, emission of initial and final radiation particles and fragmentation.

5.1.3 MadAnalysis

MadAnalysis is a framework based on C++ kernel, named SampleAnalyzer [36], which uses the Root platform. This allows to analyse events files generated by a large class of Monte Carlo event generators. This package has a reader of events files at parton-level, at hadron-level or at the reconstructed-level. Then from the information in the files the users can generate histograms illustrating various properties of the generated physical process. Moreover, all the events information from the hard-scattering process to the final-state hadrons is stored. This framework allows also the event selection using Python commands, and the tagging of each event as a background or a signal, allowing us to for an automatic treatment of the signal-over-background ratio.

5.1.4 Delphes

Delphes [37] is a C++ program that simulates the response of a detector like CMS composed of an inner tracker, electromagnetic and hadron calorimeters and a muon system. The user specifies the detector active volume, the calorimeter segmentation and the strength of the uniform magnetic field.

The particle propagation in the detector depends on the interaction of the particle with the magnetic field, that is located in the inner tracker volume. The neutral particles

follow a straight line trajectory from the production points to a calorimeter cell. In the case of a charged particles, the trajectory is helicoidal and the particle can deposit its energy in the hadronic or electromagnetic calorimeter. Particles that are outside the tracker volume are ignored. The tracking efficiency, energy and momentum resolution depend on the particle type, transverse momentum and pseudo-rapidity.

After the propagation in the magnetic field, the long-lived particles reach the calorimeters. The electromagnetic calorimeter, ECAL, measures the energy of electrons and photons. On the other hand, the hadron calorimeter, HCAL, measures the energy of long-lived charged and neutral hadrons. The calorimeters have a finite segmentation in pseudo-rapidity (η) and azimuthal angle (ϕ). The coordinate of the resulting calorimeter energy deposit, the tower, is computed as the geometrical centre of the cell. The long-lived particles deposit a fraction of their energy in the corresponding ECAL (f_{ECAL}) and HCAL (f_{HCAL}) cells. The cells of ECAL and HCAL are grouped together in the calorimeter tower. In Delphes the electrons and the photons leave all their energy in ECAL ($f_{ECAL} = 1$). Also, hadrons deposit all their energy in HCAL ($f_{HCAL} = 1$). Neutrinos, do not deposit energy in the calorimeters.

The resolution of ECAL (σ_{ECAL}) and HCAL (σ_{HCAL}) are parameterized as a function of the particle energy and pseudo-rapidity:

$$\left(\frac{\sigma}{E}\right)^2 = \left(\frac{S(\eta)}{\sqrt{E}}\right)^2 + \left(\frac{N(\eta)}{E}\right)^2 + C(\eta)^2, \tag{5.1}$$

where S, N and C are the stochastic, noise and constant terms respectively. The deposit of the electromagnetic and hadronic energy is independently smeared by a log-normal distribution ($\ln \mathcal{N}$). So the final tower energy is given as:

$$E_{Tower} = \sum_{particles} ln\mathcal{N}(f_{ECAL} \cdot E, \sigma_{ECAL}(E,\eta)) + ln\mathcal{N}(f_{HCAL} \cdot E, \sigma_{HCAL}(E,\eta)) \tag{5.2}$$

In Delphes the particle flow event reconstruction is based on the tracking system and the calorimeters. The particle flow algorithm [38] produces two collections of 4-vectors, particle flow tracks and towers; later on this is use as input for reconstructing high resolution jets and missing transverse energy. The output data is stored in a Root tree format, in such a way that it can be analyzed and visualized with the help of the Root Data Analysis.

5.2 EFT simulation

To simulate the EFT process inside MadGraph we import the model dim6top_LO_UFO [18]. The degrees of freedom of the top quark process are defined by linear combinations of the Warsaw basis operator coefficients.

Dim6top characteristics are:

- The implementation of dim6top is a tree-level one.
- Λ is fixed to 1 TeV and the EFT parameters are dimensionful coefficients $\tilde{c}_i = c_i/\Lambda^2$ expressed in units of TeV^{-2}.
- The CKM matrix is approximated as a unit matrix.
- All fermions masses and Yukawa couplings are neglected by default, except for the top and bottom quarks.
- The Goldstone boson is removed and the unitary gauge is use.
- All operator of the Warsaw basis that satisfy a U(2)q+u+d flavour symmetry and involve a top quark are included. Operators that violate baryon and lepton number are not included. In total the model includes O(90) flavour conserving degrees of freedom, which have a DIM6=1 coupling order.
- Flavour Changing Neutral Currents (FCNCs) allow a quark to break the flavour symmetry and couple the third generation with the first or the second. Operators are included with either one light and one heavy quark, one light quark one heavy quark and two leptons, one light quark and three heavy quarks, three light and one heavy quark. The degrees of freedom are assigned as FCNC=1 coupling order.

As we have seen the cross-section for the EFT has two parts, one is linear and represents the interference part with the standard model, while the other terms is a quadratic and represents the pure EFT contribution. So in order to simulate completely the EFT process we need to simulate each part. For the interference part the syntax is:

generate $pp > tt \sim$ QCD=2 FCNC=0 DIM6=1 DIM6^2==1,

and for the quadratic term is:

generate $pp > tt \sim$ QCD=2 FCNC=0 DIM6=1 DIM6^2==2.

5.3 Preliminary results

First we find the cross-section for the production of a top quark-antiquark pair in a pp collision at $\sqrt{s} = 13$ TeV, taking into account only the (SM) part. For this case we obtain a LO cross-section of 505.7± 0.8 pb. The cross-section of the standard model effective field theory (SMEFT) can be expressed as the SM value plus an additional contributions due to EFT:

$$\sigma = \sigma_{SM} + \sum_i \frac{C_i}{\Lambda^2}\tilde{\sigma}_i + \sum_{ij} \frac{C_i C_j}{\Lambda^4}\tilde{\delta}_{i,j}, \tag{5.3}$$

where $\tilde{\sigma}$ signifies the strength of the interference of the SMEFT operators with the SM, $\tilde{\delta}$ represents the pure EFT contribution, and the index i and j run over all the operators. For simulating SMEFT processes we use the dim6top model. We generate top quark-antiquark pairs including SMEFT contributions enabling separately the interference and the quadratic terms. In each case we turn on one operator at a time, setting the corresponding Wilson coefficient to a value different from zero, namely 1. The cross-section obtained for each Wilson coefficient is given in Table 5.1.

Coefficient	Interference $\sigma(pb)$	Quadratic $\sigma(pb)$
ctG	138.5 ±0.2	20.46 ± 0.04
cQq83	1.286± 0.007	1.22 ±0.003
cQq81	6.407 ± 0.012	1.226 ± 0.003
cQu8	3.847 ± 0.011	0.758 ± 0.002
cQd8	2.558 ± 0.005	0.469 ±0.001
ctq8	6.395 ± 0.015	1.223 ± 0.004
ctu8	3.849 ± 0.007	0.7549 ± 0.0018
ctd8	2.559 ± 0.005	0.4689 ± 0.0011
cQq13	1.692 ± 0.004	5.503 ±0.014
cQq11	0.4692 ± 0.0031	5.501 ±0.014
cQd1	0.1002 ± 0.0002	2.109 ±0.006
ctq1	0.3406 ± 0.0017	5.512 ± 0.015
ctu1	0.579 ± 0.001	3.41 ±0.01
ctd1	0.1916 ± 0.0004	2.111 ±0.006
cQu1	0.299 ± 0.00078	3.407 ± 0.016

TABLE 5.1: Cross-section for the interference and quadratic terms, for the different Wilson coefficients.

The relative cross-section difference due to the inclusion of the EFT terms with respect to the SM is given by

$$1000 * \frac{\sigma_{EFT}}{\sigma_{SM}}. \tag{5.4}$$

The results are shown on Table 5.2.

Coefficient	Relative difference	
	Interference	Quadratic
ctG	273.88	40.45
cQq83	2.54	2
cQq81	12.67	2.4
cQu8	7.61	1.5
cQd8	5.05	0.93
ctq8	12.65	2.4
ctu8	7.61	1.5
ctd8	5.06	0.93
cQq13	3.35	11
cQq11	0.93	11
cQd1	0.19	4.2
ctq1	0.67	11
ctu1	1.14	6.7
ctd1	0.38	4.2
cQu1	0.59	6.7

TABLE 5.2: Cross-section relative difference (in per mille).

Based on the cross-sections obtained in Table 5.1 we see that the coefficient that has the largest effect on the cross-section is ctG. Turning on only this coefficient we simulate 10,000 $t\tilde{t}$ events generated according to the SM, and as many events according the SMEFT. For the analysis we consider events with no leptons, but only jets. In this case the vetoed leptons are the electrons and muons with $|p_T| > 20$ GeV and $\eta < 2.4$, while jets are required to have $|p_T| > 30$ GeV and $|\eta| < 2.0$. We consider as variables of interest the jet multiplicity, $N(j)$, the transverse momentum p_T of the most energetic (leading) jet, and the scalar sum THT of the p_T of all jets. We fill histograms with the differential cross-section, comparing the expectation from the SM process to what obtained adding the EFT contribution. The histograms for each variables are shown in Figs. 5.2-5.4:

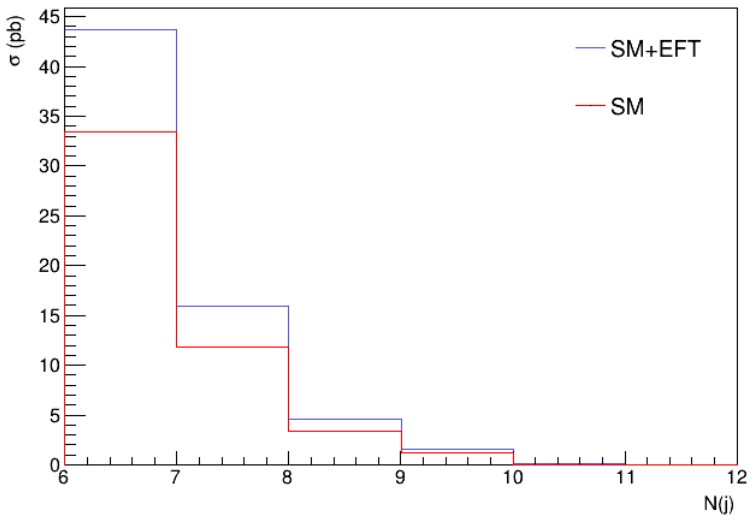

FIGURE 5.2: Differential cross-section as a function of the jet multiplicity, for SM+EFT and SM-only contributions. For the EFT contribution, only the ctG coefficient is considered.

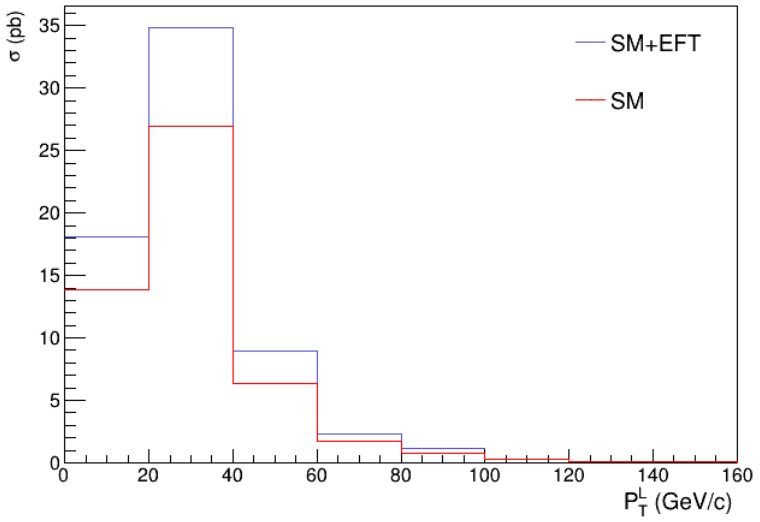

FIGURE 5.3: Differential cross-section as a function of the transverse momentum of the leading jet, for SM+EFT and SM-only contributions. For the EFT contribution, only the ctG coefficient is considered.

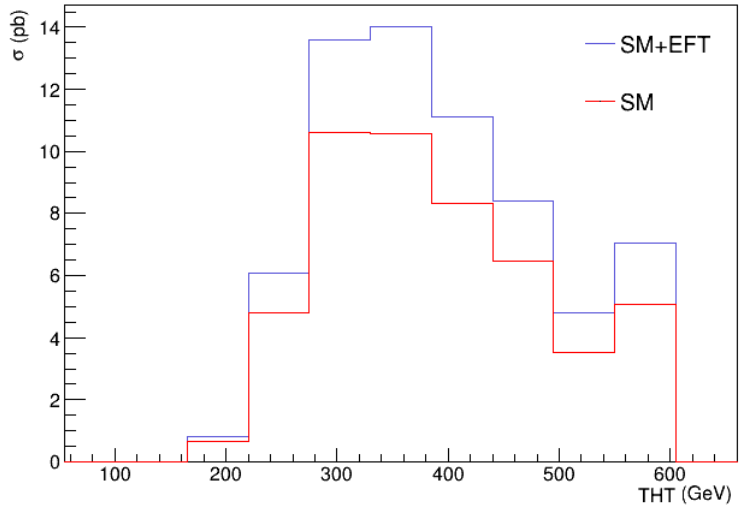

FIGURE 5.4: Differential cross-section as a function of the scalar sum THT, for SM+EFT and SM-only contributions. For the EFT contribution, only the ctG coefficient is considered.

To highlight the effect of EFT, we plot, for the same variables, the cross-section ratio defined as:

$$R = \frac{\sigma(SM + EFT)}{\sigma(SM)}. \tag{5.5}$$

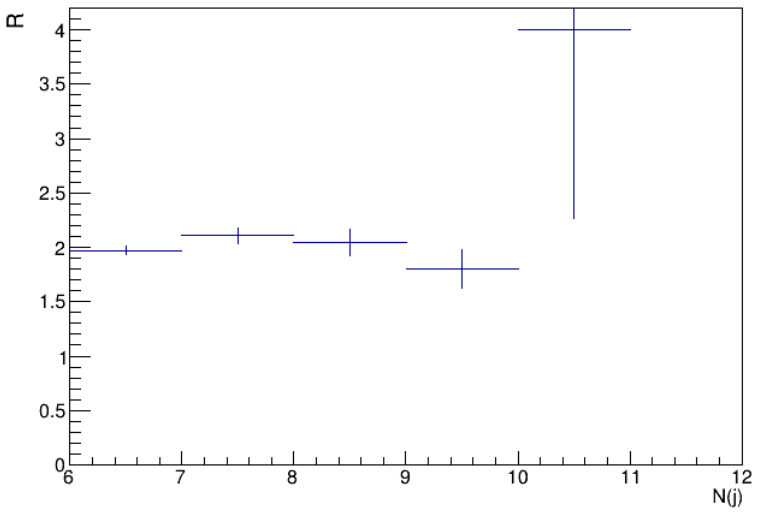

FIGURE 5.5: Cross-section ratio vs the jet multiplicity (for ctG=1).

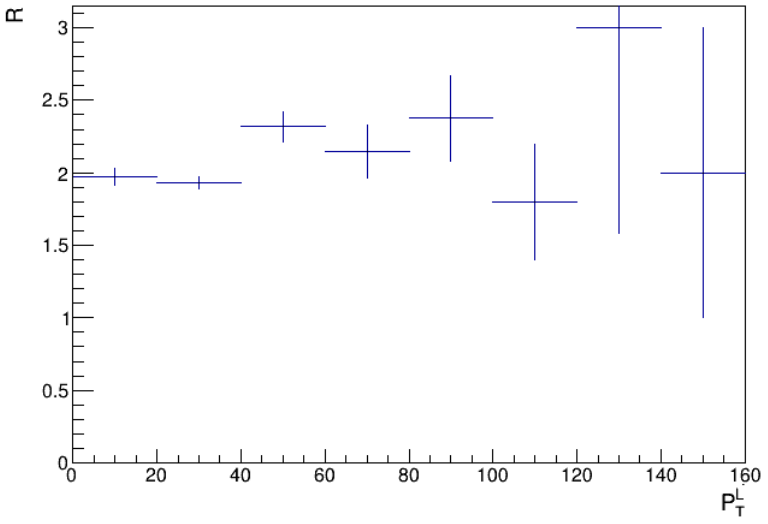

FIGURE 5.6: Cross-section ratio vs the transverse momentum of the leading jet (for ctG=1).

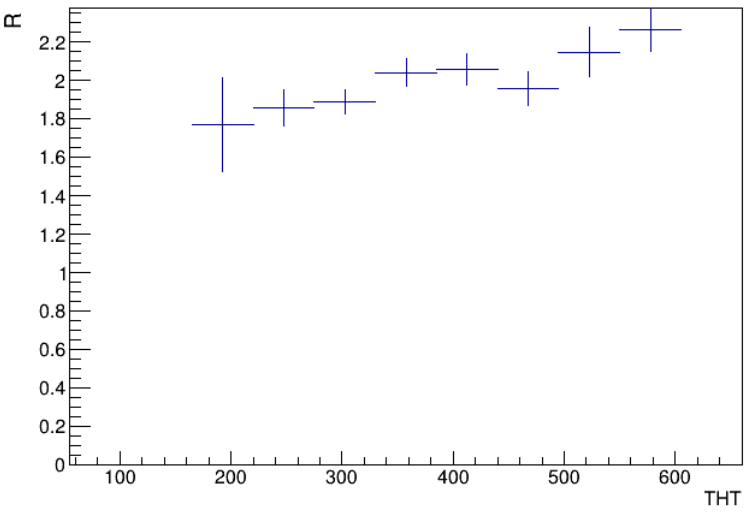

FIGURE 5.7: Cross-section ratio vs THT (for ctG=1).

We repeat the same analysis for the next most relevant coefficients, cQq81 and ctq8. In Figs. 5.8- 5.10 we show the histograms for the chosen variables, setting cQq81=5 to enhance the EFT contribution.

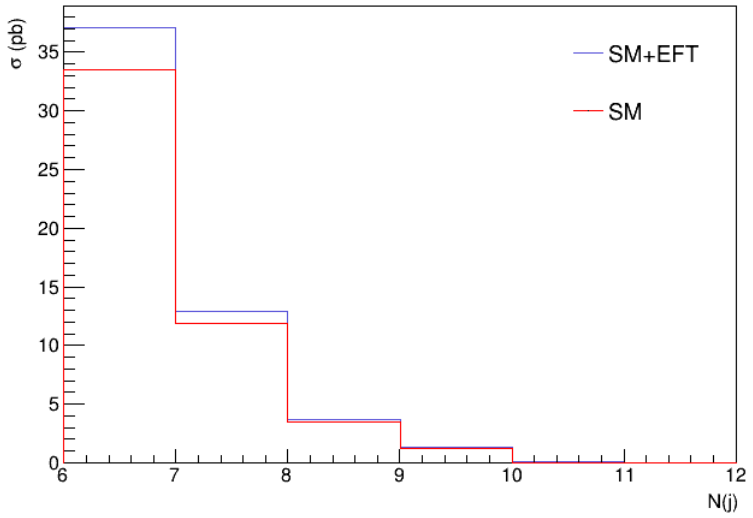

FIGURE 5.8: Differential cross-section as a function of the jet multiplicity, for SM+EFT and SM-only contributions. For the EFT contribution, only the cQq81 coefficient is considered.

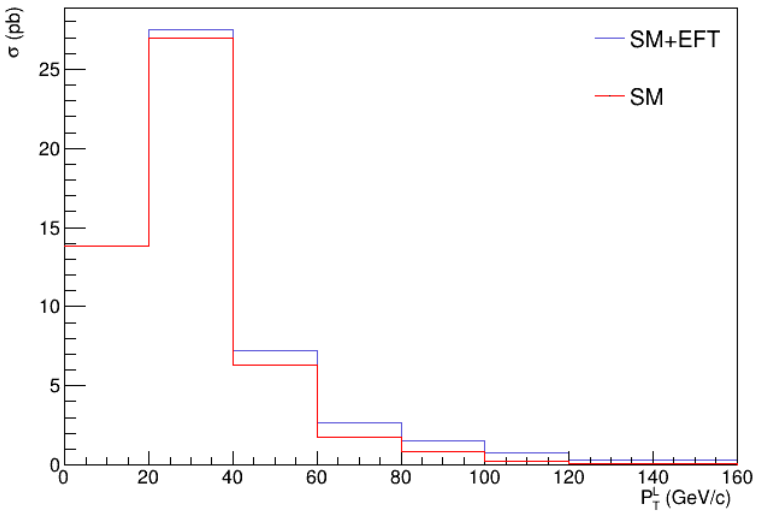

FIGURE 5.9: Differential cross-section as a function of transverse momentum of the leading jet, for SM+EFT and SM-only contributions. For the EFT contribution, only cQq81 the coefficient is considered.

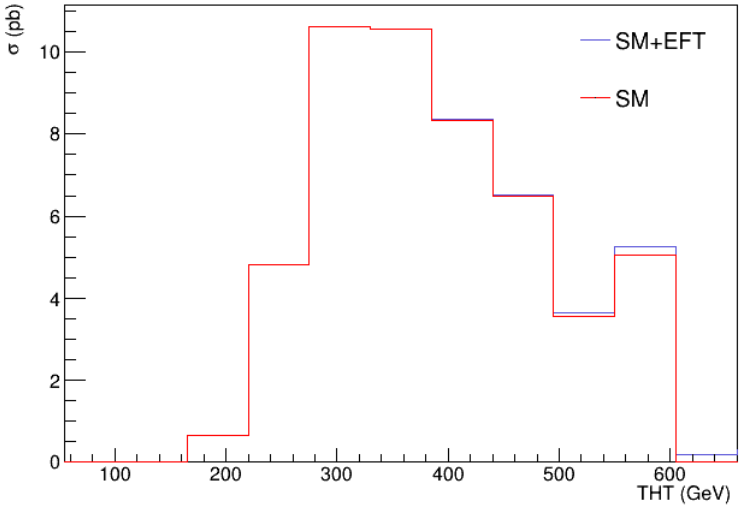

FIGURE 5.10: Differential cross-section as a function of THT, for SM+EFT and SM-only contributions. For the EFT contribution, only the cQq81 coefficient is considered.

The corresponding cross-section ratios are shown in Figs. 5.11-5.13.

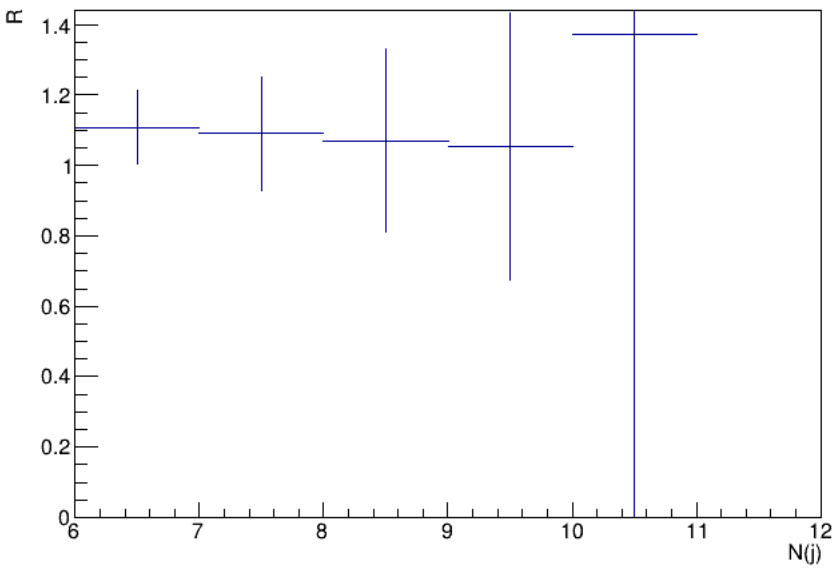

FIGURE 5.11: Cross-section ratio vs the jet multiplicity (for cQq81=5).

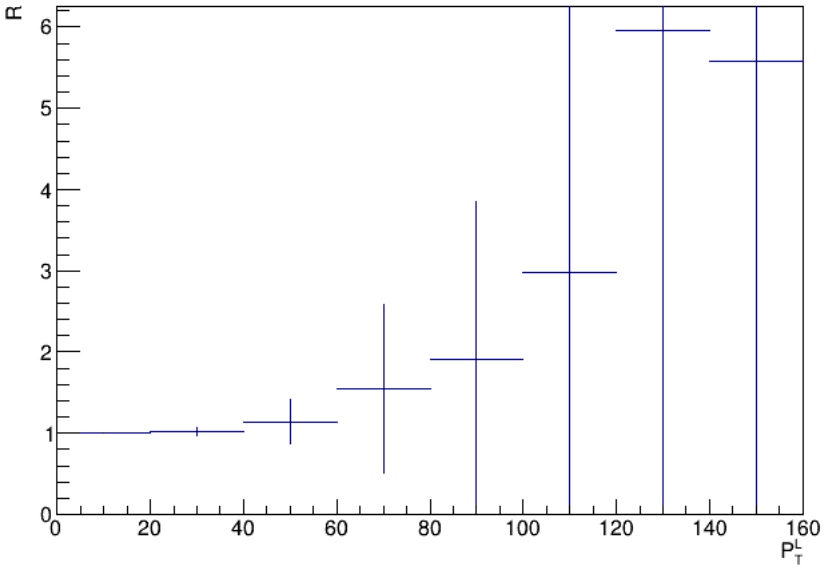

FIGURE 5.12: Cross-section ratio vs the transverse momentum of the leading jet (for cQq81=5).

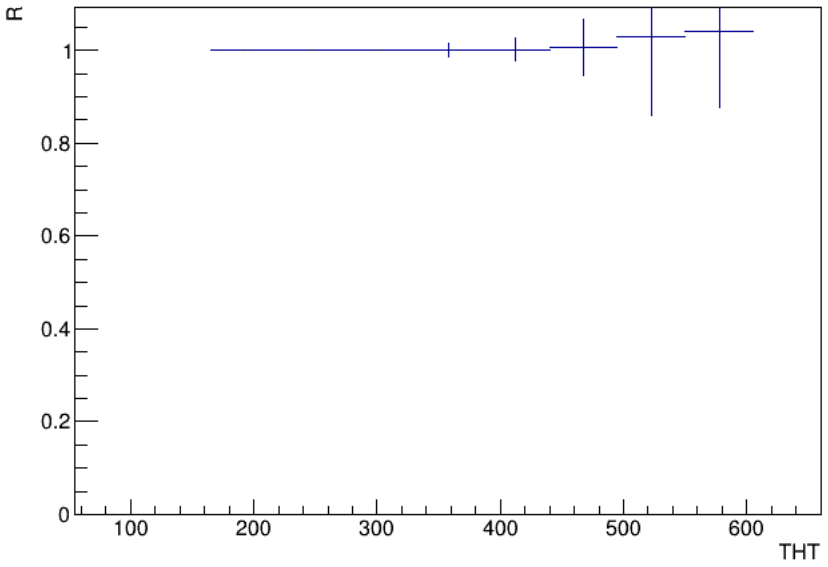

FIGURE 5.13: Cross-section ratio vs the THT (for cQq81=5).

The cross-section comparison for each variable in the case of ctq8=5 are shown in Figs. 5.14- 5.16, with the ratios shown in Figs. 5.17-5.19.

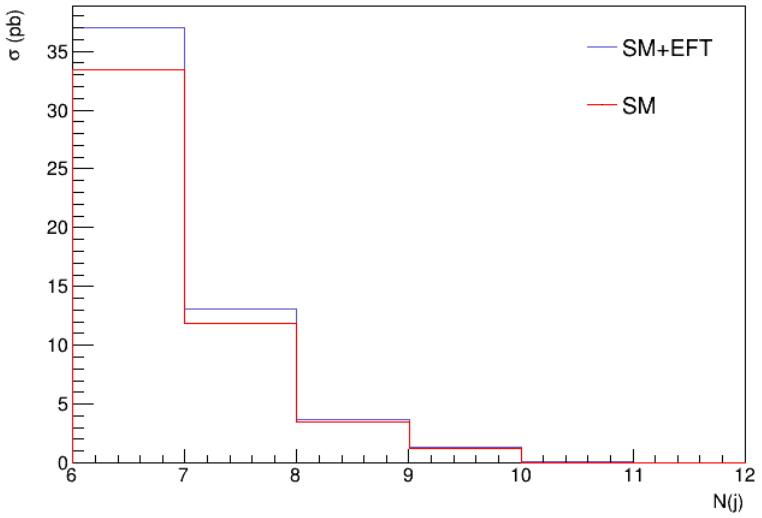

FIGURE 5.14: Differential cross-section as a function of the jet multiplicity, for SM+EFT and SM-only contributions. For the EFT contribution, only the ctq8 coefficient is considered.

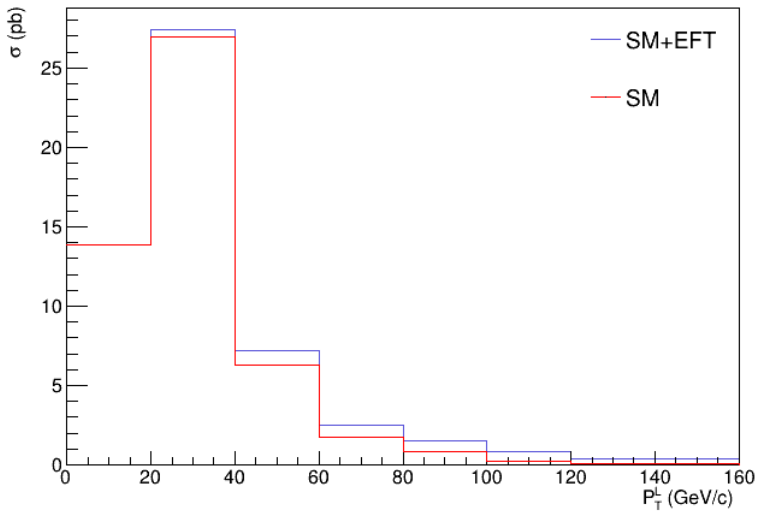

FIGURE 5.15: Differential cross-section as a function of transverse momentum of the leading jet, for SM+EFT and SM-only contributions. For the EFT contribution, only the ctq8 coefficient is considered.

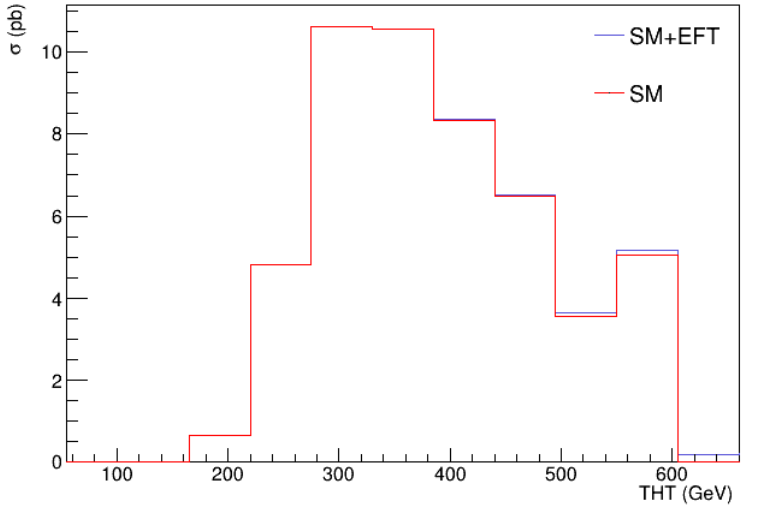

FIGURE 5.16: Differential cross-section as a function of THT, for SM+EFT and SM-only contributions. For the EFT contribution, only the ctq8 coefficient is considered.

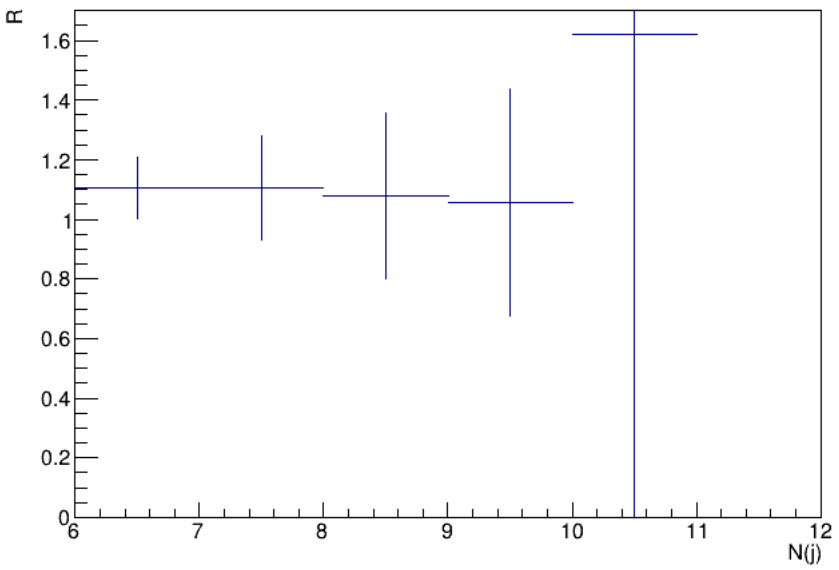

FIGURE 5.17: Cross-section ratio vs the jet multiplicity (for ctq8=5).

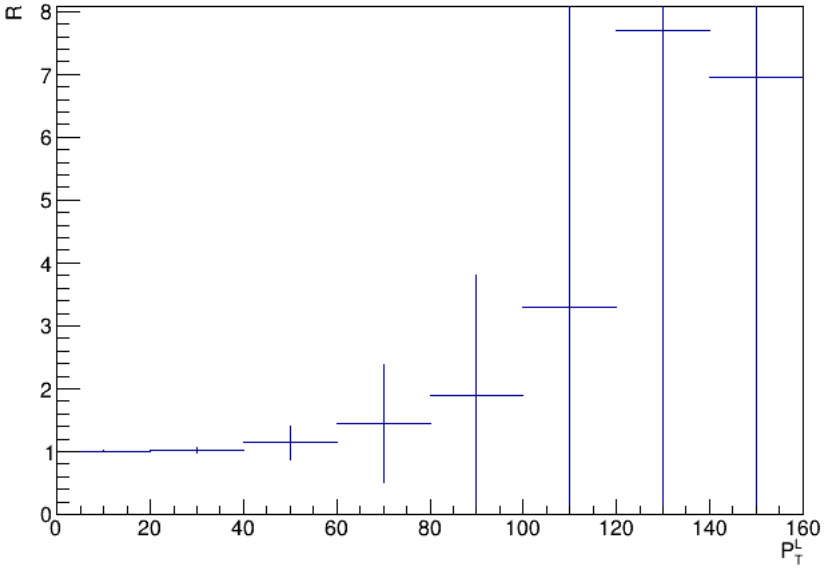

FIGURE 5.18: Cross-section ratio vs the transverse momentum of the leading jet (for ctq8=5).

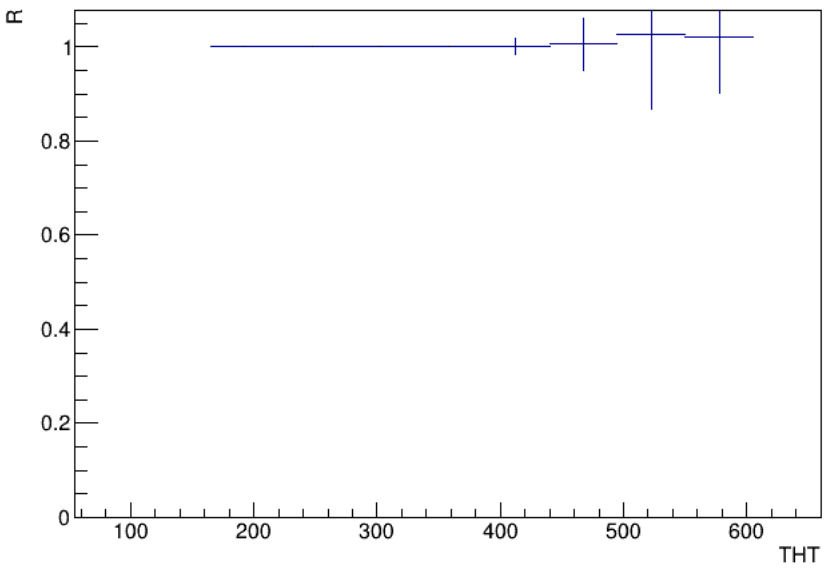

FIGURE 5.19: Cross-section ratio vs THT (for ctq8=5).

Chapter 6

Analysis

The preliminary results shown in the previous chapter, clearly indicates the need for a more detailed study. To this purpose we improve the analysis by:

- Increasing the number of simulated events;
- Separating the commonly defined final states.

For this analysis we generate 100,000 events of $pp \to t\bar{t}$ for the SM and for the EFT separately. For the EFT process we only select one Wilson coefficient at a time, assigning to it different values. For this case we select the Wilson coefficient that we found more relevant in the preliminary results, which are the ctG, cQq81 and ctq8. The respective cross-section for each $t\bar{t}$ process is shown in Table 6.1

Process	Cross-section (pb)	Difference relative to SM (in per mille)
SM	505.7	-
ctG=1	158.69	313.8
cQq81=1	7.64	15.1
ctq8=1	7.61	15.04
cQq81=5	62.69	123.97
ctq8=5	62.67	123.93

TABLE 6.1: Cross-section for the different processes, and the relative difference with respect to the SM.

We do the analysis for the three possible decays: the all-hadronic, the single lepton and the dileptonic.

6.1 At hadron/particle level

6.1.1 All-hadronic final state

This channel is defined by the following requirements:

- No leptons (e or mu) with $p_T > 20$ GeV and $|\eta| < 2.4$;
- at least 6 jets having a $p_T > 30$ GeV and $|\eta| < 2.0$.

Differential cross sections are determined in the following for the same variables introduced in the previous chapter, i.e. the jet multiplicity, the p_T of the leading jet and the scalar sum THT, considering the most relevant Wilson coefficients ctG, cQq81 and ctq8. Cross sections after the event selection for this channel are summarized in Table 6.2

Process	Cross-section (pb)	Difference relative to SM (in per mille)
SM	49.32	-
ctG=1	16.30	330.49
cQq81=5	5.02	101.78
ctq8=5	5.44	110.30

TABLE 6.2: Cross-section for the hadronic channel for the different processes, and the relative difference with respect to the SM.

Differential cross sections and ratios are shown in Figs. 6.1-6.6 for the ctG, in Figs. 6.7-6.12 for the cQq81, and in Figs. 6.13-6.18 for the ctq8. For the ratios, a linear fit is applied, to show the possible indication of a trend in the distribution.

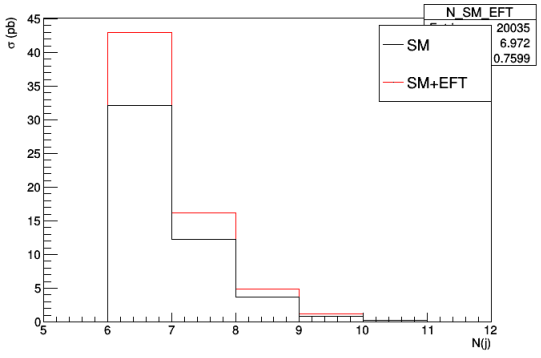

FIGURE 6.1: Differential cross section as a function of the jet multiplicity, in the all-hadronic state, for the ctG coefficient.

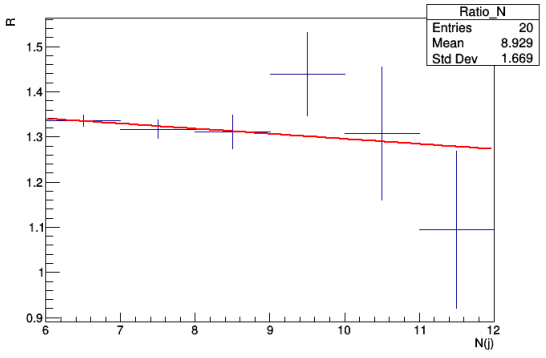

FIGURE 6.2: Cross section ratio as a function of the jet multiplicity,in the all-hadronic state, for the ctG coefficient.

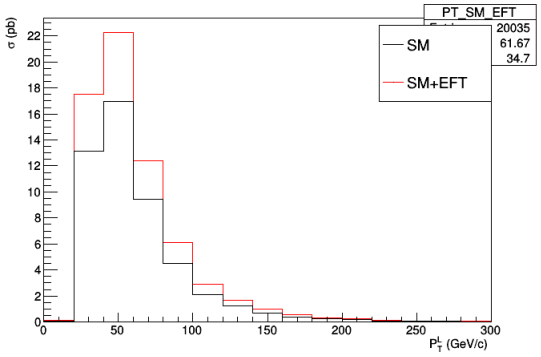

FIGURE 6.3: Differential cross section as a function of the transverse momentum of the leading jet, in the all-hadronic state, for the ctG coefficient.

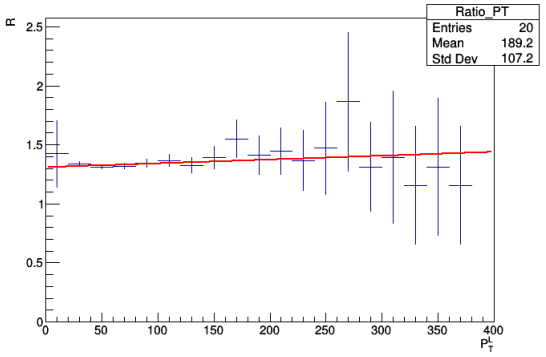

FIGURE 6.4: Cross section ratio as a function of the transverse momentum of the leading jet,in the all-hadronic state, for the ctG coefficient.

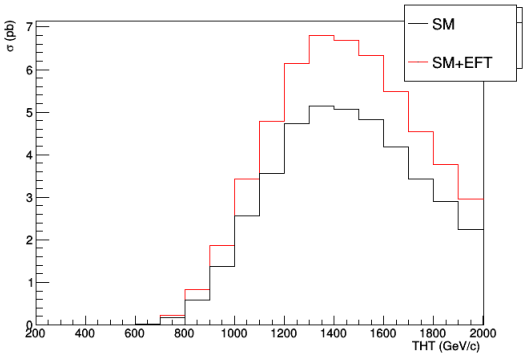

FIGURE 6.5: Differential cross section as a function of the THT variable, in the all-hadronic state, for the ctG coefficient.

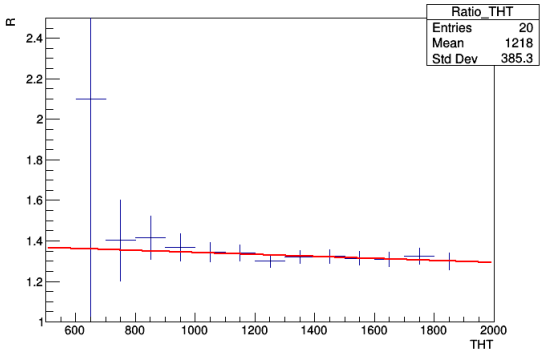

FIGURE 6.6: Cross section ratio as a function of the THT variable,in the all-hadronic state, for the ctG coefficient.

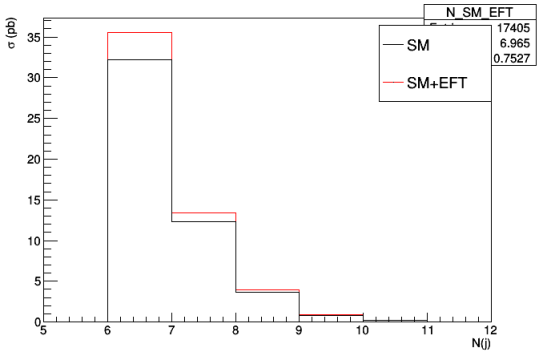

FIGURE 6.7: Differential cross section as a function of the jet multiplicity, in the all-hadronic state, for the cQq81 coefficient.

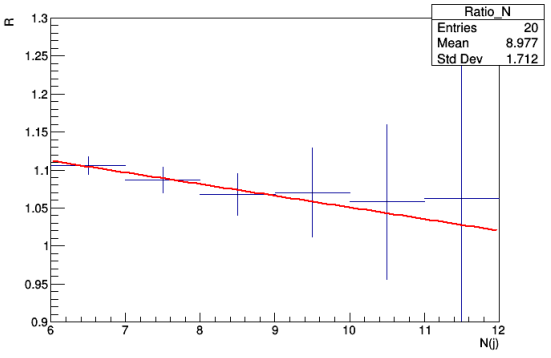

FIGURE 6.8: Cross section ratio as a function of the jet multiplicity,in the all-hadronic state, for the cQq81 coefficient.

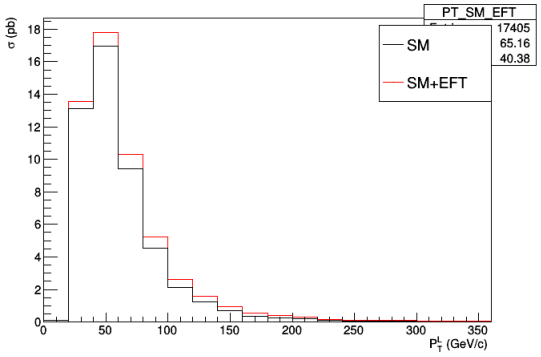

FIGURE 6.9: Differential cross section as a function of the transverse momentum of the leading jet, in the all-hadronic state, for the cQq81 coefficient.

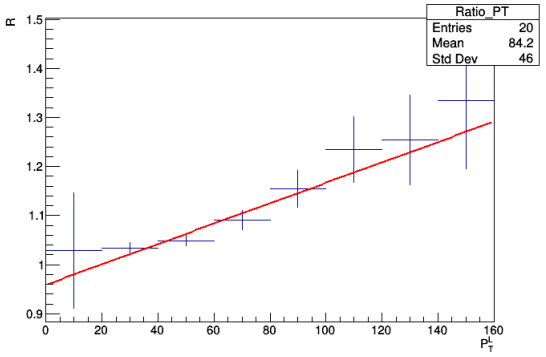

FIGURE 6.10: Cross section ratio as a function of the transverse momentum of the leading jet,in the all-hadronic state, for the cQq81 coefficient.

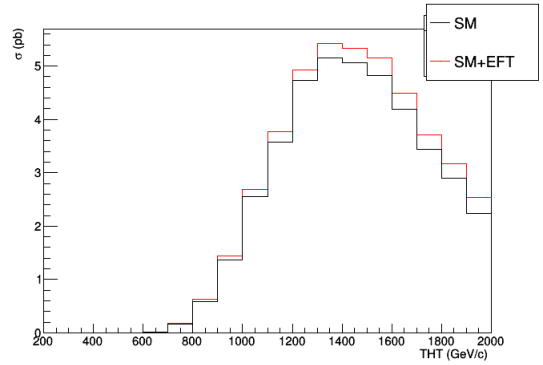

FIGURE 6.11: Differential cross section as a function of the THT variable, in the all-hadronic state, for the cQq81 coefficient.

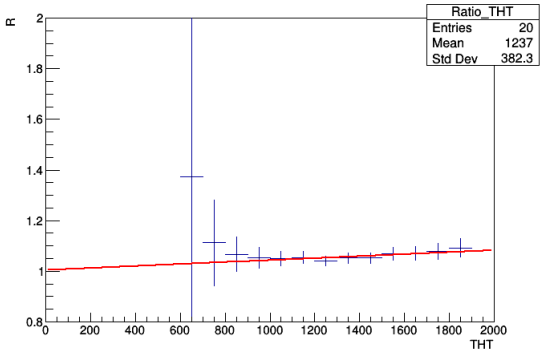

FIGURE 6.12: Cross section ratio as a function of the THT variable, in the all-hadronic state, for the cQq81 coefficient.

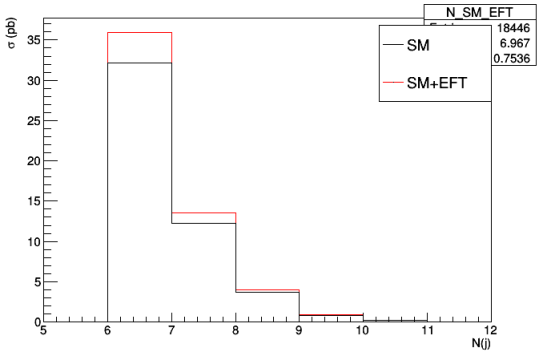

FIGURE 6.13: Differential cross section as a function of the jet multiplicity, in the all-hadronic state, for the ctq8 coefficient.

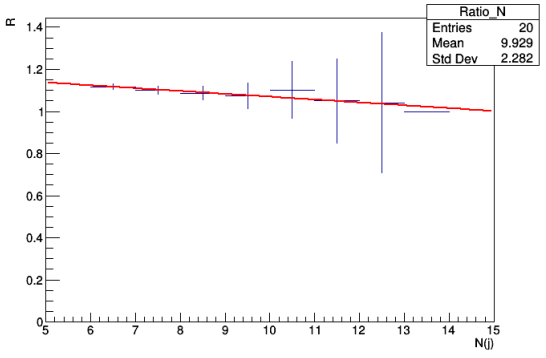

FIGURE 6.14: Cross section ratio as a function of the jet multiplicity, in the all-hadronic state, for the ctq8 coefficient.

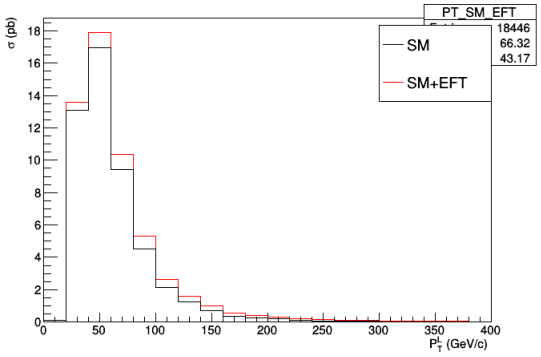

FIGURE 6.15: Differential cross section as a function of the transverse momentum of the leading jet, in the all-hadronic state, for the ctq8 coefficient.

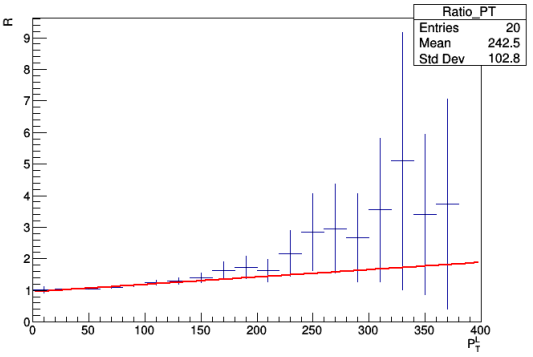

FIGURE 6.16: Cross section ratio as a function of the transverse momentum of the leading jet, in the all-hadronic state, for the ctq8 coefficient.

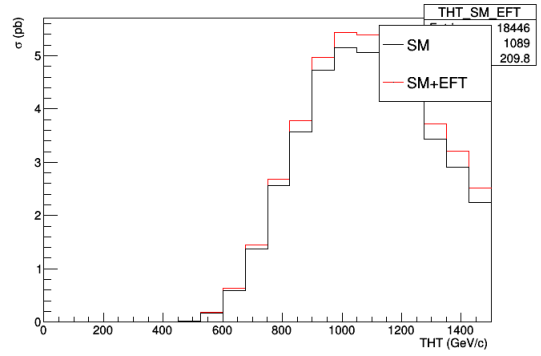

FIGURE 6.17: Differential cross section as a function of the THT variable, in the all-hadronic state, for the ctq8 coefficient.

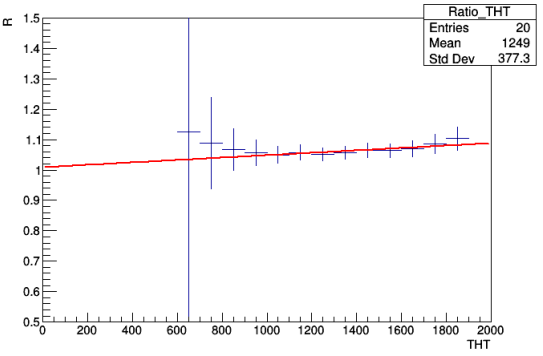

FIGURE 6.18: Cross section ratio as a function of the THT variable, in the all-hadronic state, for the ctq8 coefficient.

6.1.2 The semi-leptonic process

This channel is defined by the following requirements:

- A single lepton (e or mu) with $p_T > 20$ GeV and $|\eta| < 2.4$;
- at least 4 jets having a $p_T > 30$ GeV and $|\eta| < 2.0$.

Differential cross sections are determined in the following for the same variables introduced in the previous chapter, i.e. the p_T of the leading lepton and the scalar sum THT, considering the most relevant Wilson coefficients ctG, cQq81 and ctq8. Cross sections after the event selection for this channel are summarized in Table 6.3

Process	Cross-section (pb)	Difference relative to SM (in per mille)
SM	48.49	-
ctG=1	15.66	322.95
cQq81=5	5.84	120.44
ctq8=5	6.12	126.21

TABLE 6.3: Cross-section for the semi-leptonic channel for the different processes, and the relative difference with respect to the SM.

Differential cross sections and ratios are shown in Figs. 6.19-6.22 for the ctG, in Figs. 6.23-6.26 for the cQq81, and in Figs. 6.27-6.30 for the ctq8. For the ratios, a linear fit is applied, to show the possible indication of a trend in the distribution.

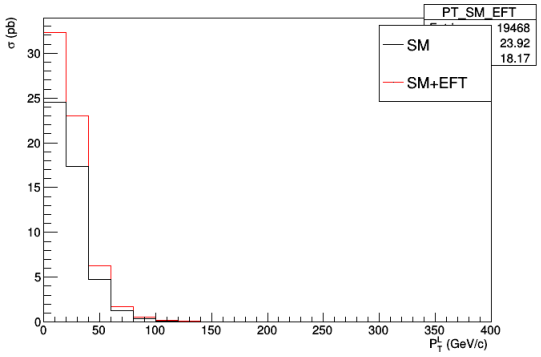

FIGURE 6.19: Differential cross section as a function of the transverse momentum of the leading lepton, in the semi-leptonic state, for the ctG coefficient.

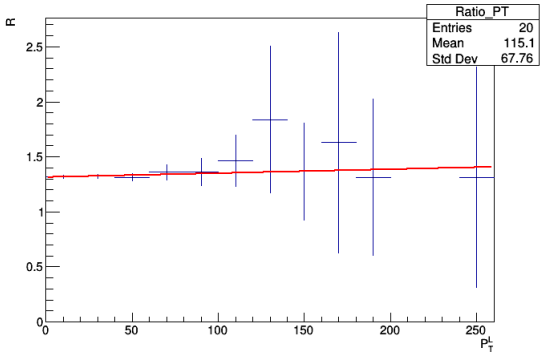

FIGURE 6.20: Cross section ratio as a function of the transverse momentum of the leading lepton, in the semi-leptonic state, for the ctG coefficient.

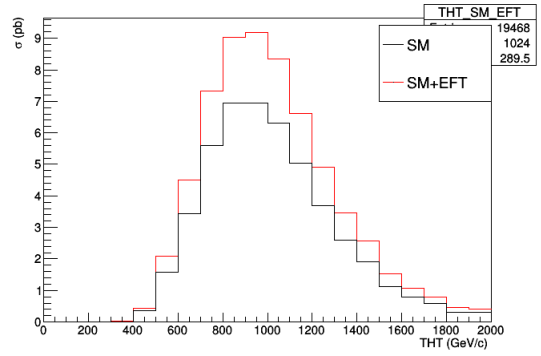

FIGURE 6.21: Differential cross section as a function of the THT variable, in the semi-leptonic state, for the ctG coefficient.

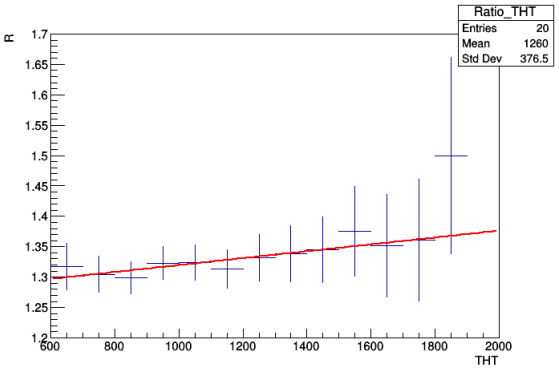

FIGURE 6.22: Cross section ratio as a function of the THT variable, in the semi-leptonic state, for the ctG coefficient.

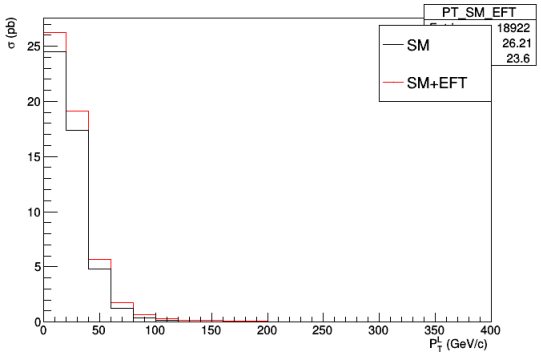

FIGURE 6.23: Differential cross section as a function of the transverse momentum of the leading lepton, in the semi-leptonic state, for the cQq81 coefficient.

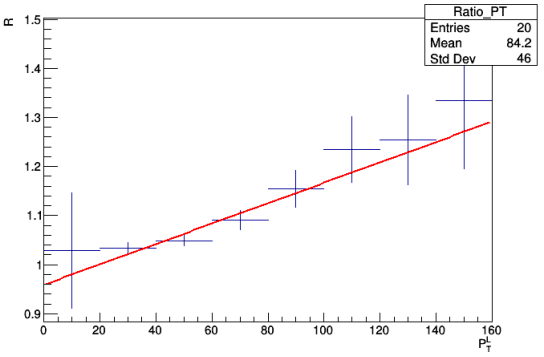

FIGURE 6.24: Cross section ratio as a function of the transverse momentum of the leading lepton, in the semi-leptonic state, for the cQq81 coefficient.

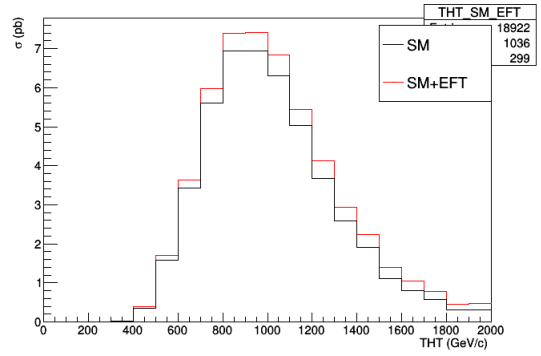

FIGURE 6.25: Differential cross section as a function of the THT variable, in the semi-leptonic state, for the cQq81 coefficient.

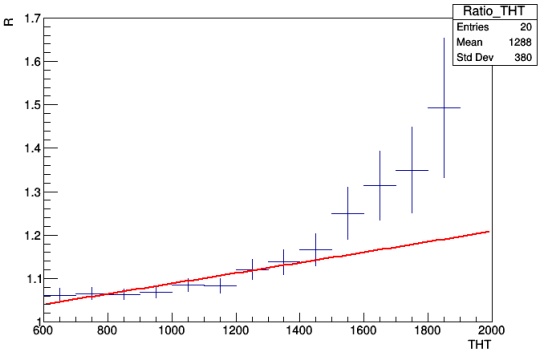

FIGURE 6.26: Cross section ratio as a function of the THT variable, in the semi-leptonic state, for the cQq81 coefficient.

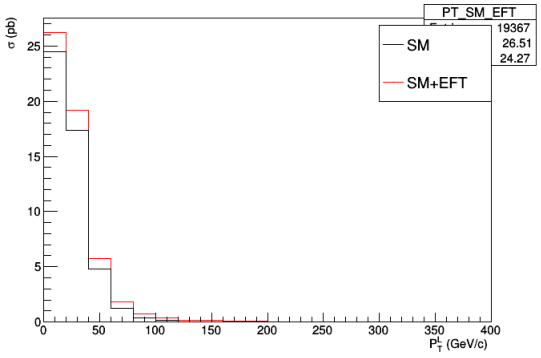

FIGURE 6.27: Differential cross section as a function of the transverse momentum of the leading lepton, in the semi-leptonic state, for the ctq8 coefficient.

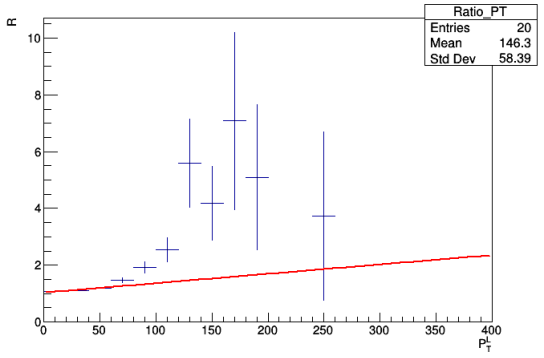

FIGURE 6.28: Cross section ratio as a function of the transverse momentum of the leading lepton, in the semi-leptonic state, for the ctq8 coefficient.

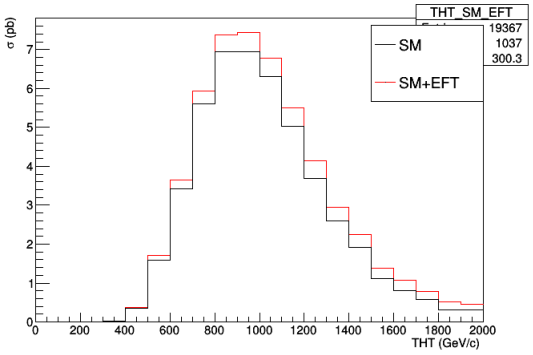

FIGURE 6.29: Differential cross section as a function of the THT variable, in the semi-leptonic state, for the ctq8 coefficient.

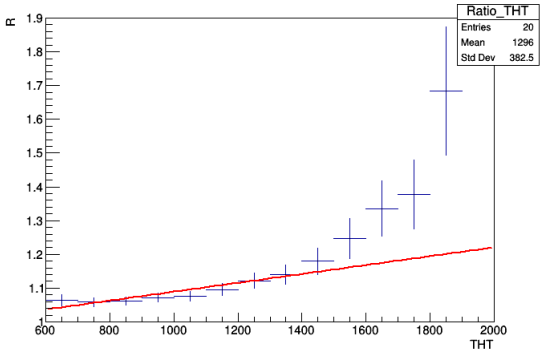

FIGURE 6.30: Cross section ratio as a function of the THT variable, in the semi-leptonic state, for the ctq8 coefficient.

6.1.3 The dileptonic process

This channel is defined by the following requirements:

- Two leptons (e or mu) with $p_T > 20$ GeV and $|\eta| < 2.4$;
- at least 2 jets having a $p_T > 30$ GeV and $|\eta| < 2.0$.

Differential cross sections are determined in the following for the same variables introduced in the previous chapter, i.e. the p_T of the leading lepton and the scalar sum THT, considering the most relevant Wilson coefficients ctG, cQq81 and ctq8. Cross sections after the event selection for this channel are summarized in Table 6.4

Process	Cross-section (pb)	Difference relative to SM (in per mille)
SM	21.89	-
ctG=1	7.58	346.28
cQq81=5	3.39	154.86
ctq8=5	3.42	156.24

TABLE 6.4: Cross-section for the dileptonic channel for the different processes, and the relative difference with respect to the SM.

Differential cross sections and ratios are shown in Figs. 6.31-6.34 for the ctG, in Figs. 6.35-6.38 for the cQq81, and in Figs. 6.39-6.42 for the ctq8. For the ratios, a linear fit is applied, to show the possible indication of a trend in the distribution.

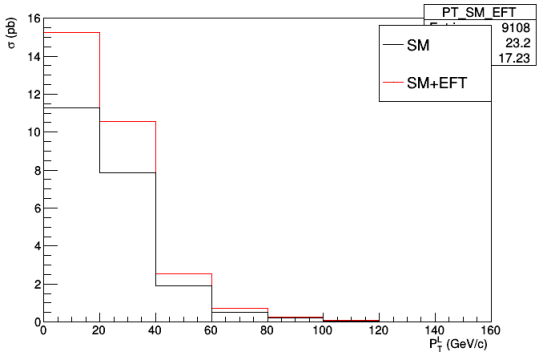

FIGURE 6.31: Differential cross section as a function of the transverse momentum of the leading lepton, in the dileptonic state, for the ctG coefficient.

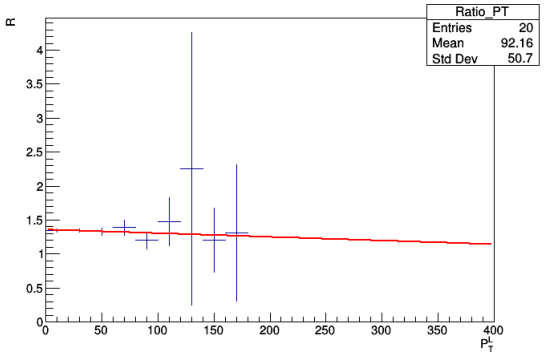

FIGURE 6.32: Cross section ratio as a function of the transverse momentum of the leading lepton, in the dileptonic state, for the ctG coefficient.

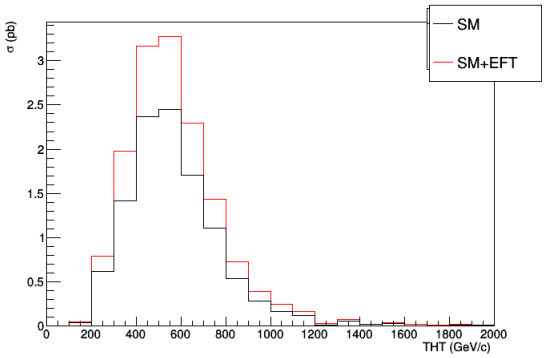

FIGURE 6.33: Differential cross section as a function of the THT variable, in the dileptonic state, for the ctG coefficient.

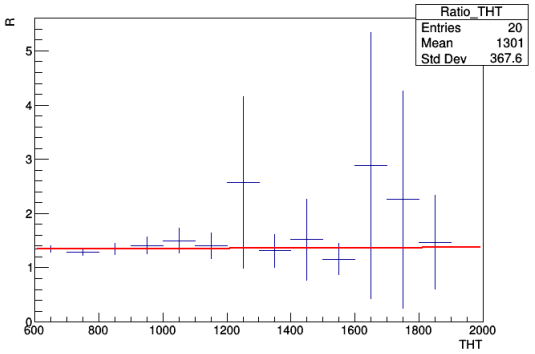

FIGURE 6.34: Cross section ratio as a function of the THT variable, in the dileptonic state, for the ctG coefficient.

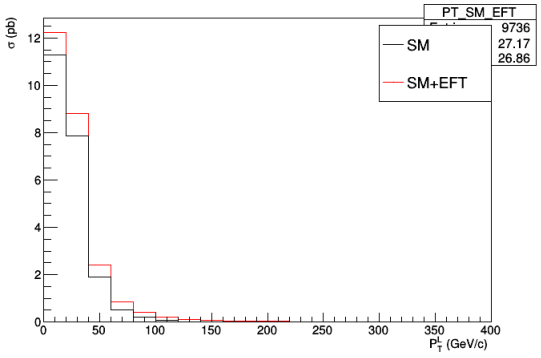

FIGURE 6.35: Differential cross section as a function of the transverse momentum of the leading lepton, in the dileptonic state, for the cQq81 coefficient.

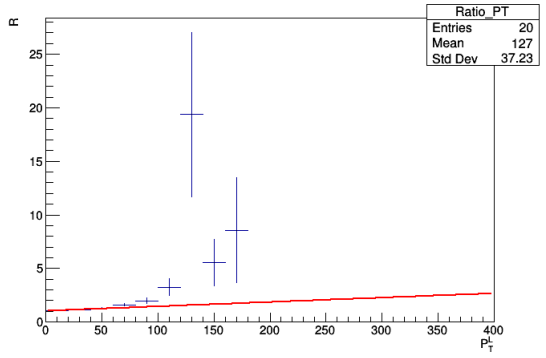

FIGURE 6.36: Cross section ratio as a function of the transverse momentum of the leading lepton, in the dileptonic state, for the cQq81 coefficient.

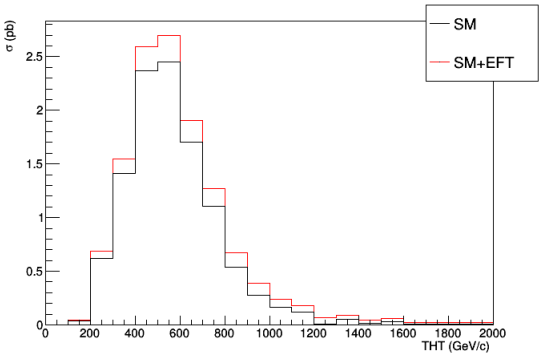

FIGURE 6.37: Differential cross section as a function of the THT variable, in the dileptonic state, for the cQq81 coefficient.

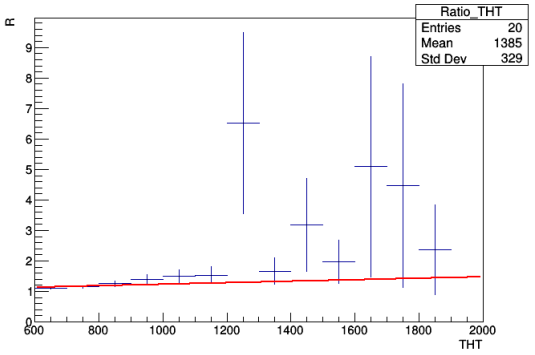

FIGURE 6.38: Cross section ratio as a function of the THT variable, in the dileptonic state, for the cQq81 coefficient.

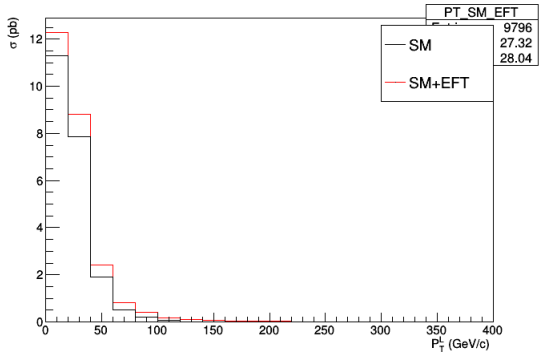

FIGURE 6.39: Differential cross section as a function of the transverse momentum of the leading lepton, in the dileptonic state, for the ctq8 coefficient.

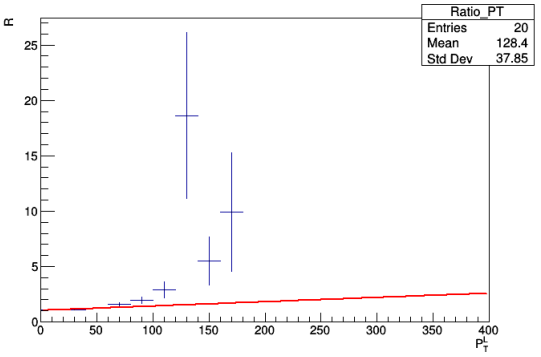

FIGURE 6.40: Cross section ratio as a function of the transverse momentum of the leading lepton, in the dileptonic state, for the ctq8 coefficient.

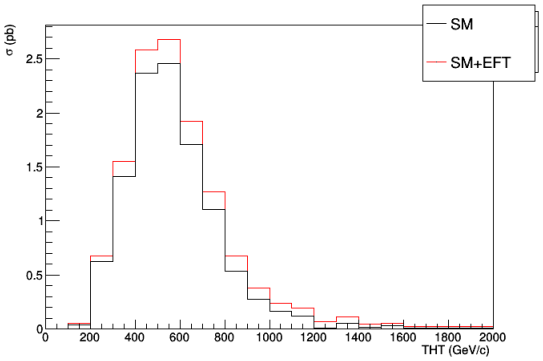

FIGURE 6.41: Differential cross section as a function of the THT variable, in the dileptonic state, for the ctq8 coefficient.

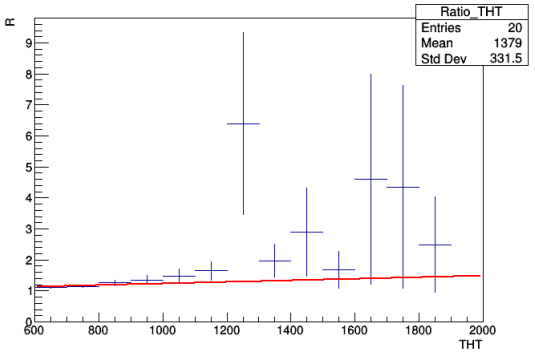

FIGURE 6.42: Cross section ratio as a function of the THT variable, in the dileptonic state, for the ctq8 coefficient.

6.2 Analysis at detector level

The final states are defined as for the analysis at particle level, and with the same thresholds for lepton and jets.

6.2.1 All-hadronic

We defined this channel the same way as we did for the all-hadronic channel at particle level.

The differential cross-section after the event selection for SM and EFT for this channel are summarized in Table 6.5

Process	Cross-section (pb)	Difference relative to SM (in per mille)
SM	65.28	-
ctG=1	21.48	329.04
cQq81=5	4.85	74.29
ctq8=5	5.52	84.56

TABLE 6.5: Cross-section for the hadronic channel for the different processes at detector level, and the relative difference with respect to the SM.

Differential cross sections and ratios are shown in Figs. 6.43-6.48 for the ctG, in Figs. 6.49-6.54 for the cQq81, and in Figs. 6.55-6.60 for the ctq8. For the ratios, a linear fit is applied, to show the possible indication of a trend in the distribution.

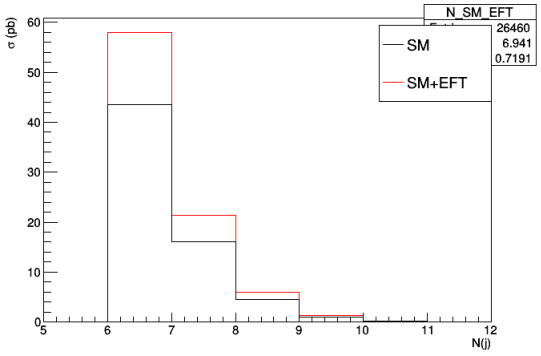

FIGURE 6.43: Differential cross section as a function of the jet multiplicity, in the all-hadronic state, for the ctG coefficient.

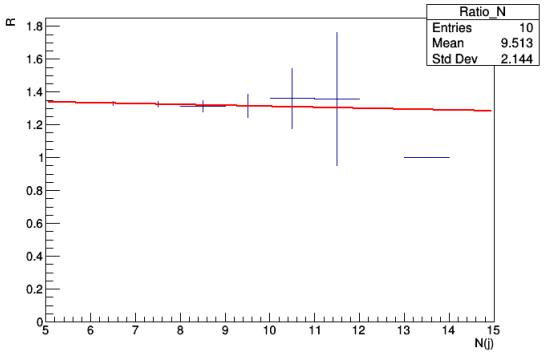

FIGURE 6.44: Cross section ratio as a function of the jet multiplicity,in the all-hadronic state, for the ctG coefficient.

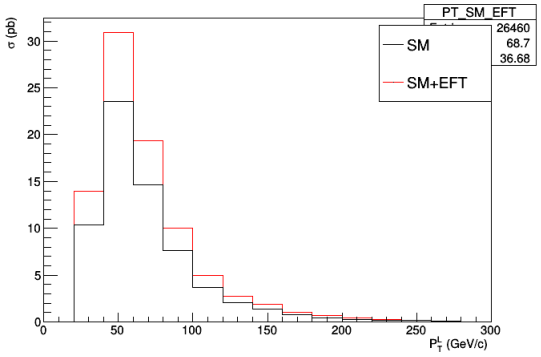

FIGURE 6.45: Cross section as a function of the transverse momentum of the leading jet, in the all-hadronic state, for the ctG coefficient.

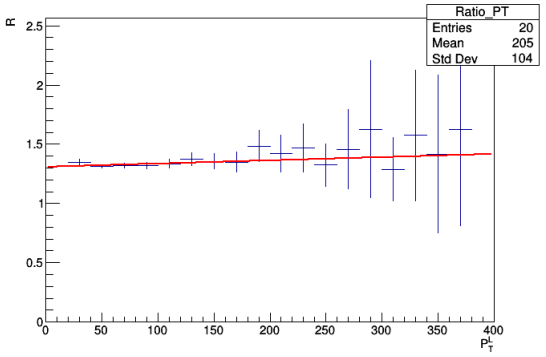

FIGURE 6.46: Cross section ratio as a function of the transverse momentum of the leading jet, in the all-hadronic state, for the ctG coefficient.

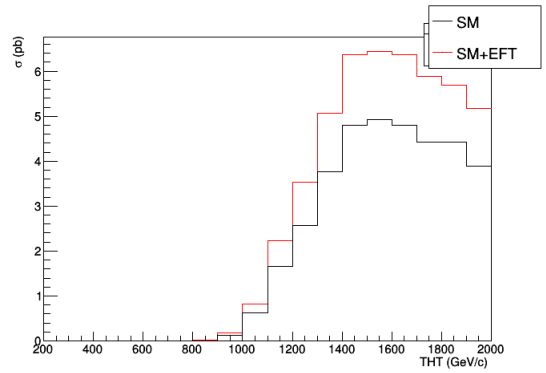

FIGURE 6.47: Differential cross section as a function of the THT variable, in the all-hadronic state, for the ctG coefficient.

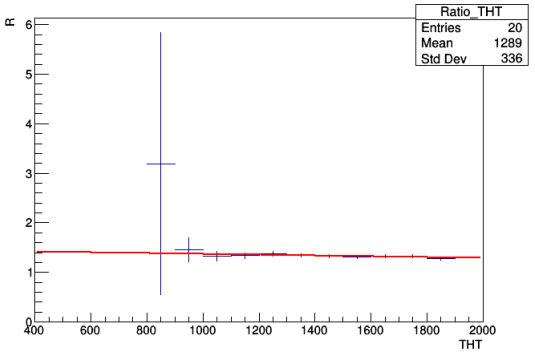

FIGURE 6.48: Cross section ratio as a function of the THT variable, in the all-hadronic state, for the ctG coefficient.

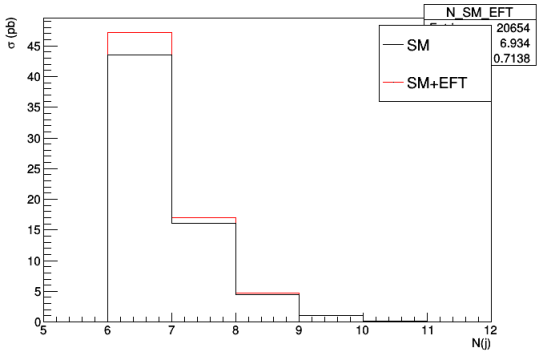

FIGURE 6.49: Differential cross section as a function of the jet multiplicity, in the all-hadronic state, for the cQq81 coefficient.

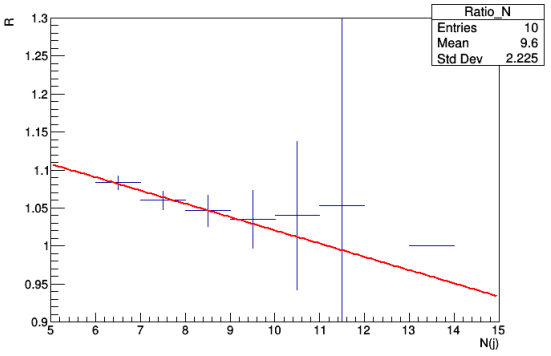

FIGURE 6.50: Cross section ratio as a function of the the jet multiplicity, in the all-hadronic state, for the cQq81 coefficient.

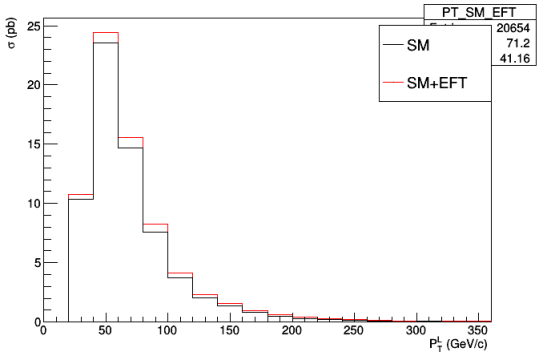

FIGURE 6.51: Differential cross section as a function of the transverse momentum of the leading jet, in the all-hadronic state, for the cQq81 coefficient.

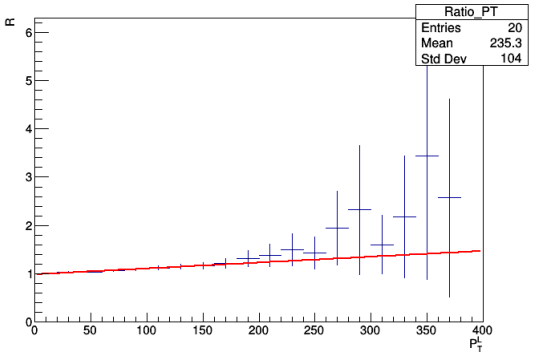

FIGURE 6.52: Cross section ratio as a function of the transverse momentum of the leading jet, in the all-hadronic state, for the cQq81 coefficient.

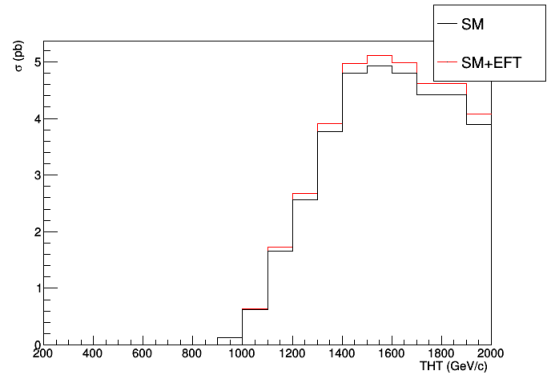

FIGURE 6.53: Differential cross section as a function of the THT variable, in the all-hadronic state, for the cQq81 coefficient.

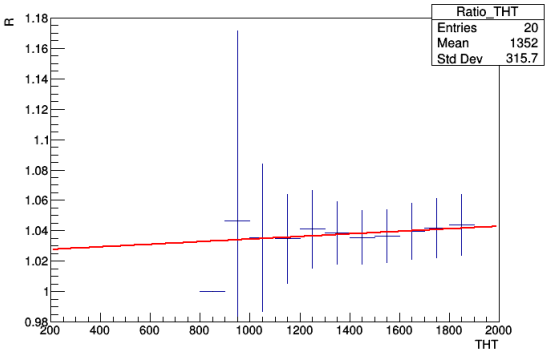

FIGURE 6.54: Cross section ratio as a function of the THT variable, in the all-hadronic state, for the cQq81 coefficient.

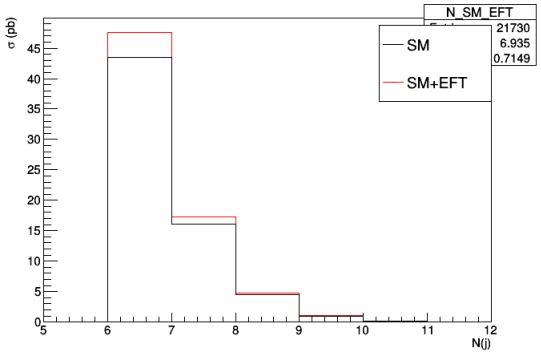

FIGURE 6.55: Differential cross section as a function of the jet multiplicity, in the all-hadronic state, for the ctq8 coefficient.

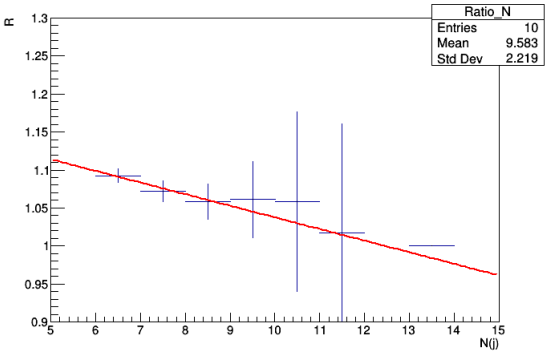

FIGURE 6.56: Cross section ratio as a function of the jet multiplicity, in the all-hadronic state, for the ctq8 coefficient.

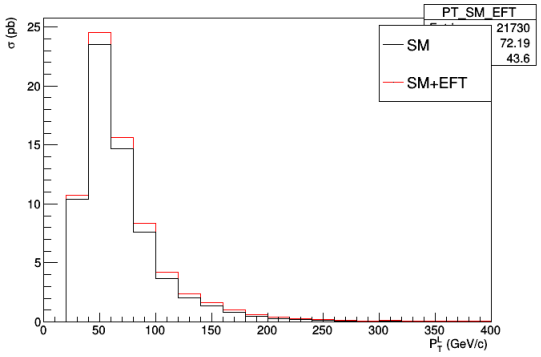

FIGURE 6.57: Differential cross section as a function of the transverse momentum of the leading jet, in the all-hadronic state, for the ctq8 coefficient.

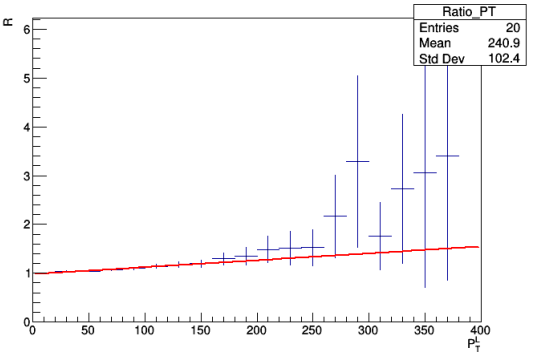

FIGURE 6.58: Cross section ratio as a function of the transverse momentum of the leading jet, in the all-hadronic state, for the ctq8 coefficient.

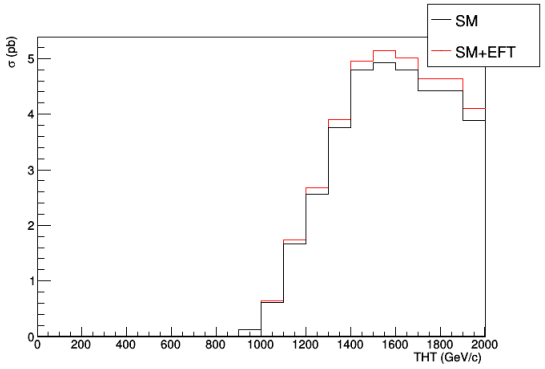

FIGURE 6.59: Differential cross section as a function of the THT variable, in the all-hadronic state, for the ctq8 coefficient.

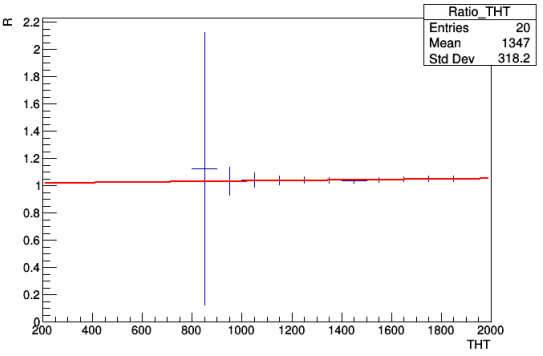

FIGURE 6.60: Cross section ratio as a function of the THT variable, in the all-hadronic state, for the ctq8 coefficient.

6.2.2 Semi-leptonic process

We defined this channel the same way as we did for the semi-leptonic channel at particle level.

The differential cross-section after the event selection for SM and EFT for this channel are summarized in Table 6.6

Process	Cross-section (pb)	Difference relative to SM (in per mille)
SM	37.02	-
ctG=1	11.77	317.94
cQq81=5	3.09	83.47
ctq8=5	3.32	89.68

TABLE 6.6: Cross-section for the semi-leptonic channel for the different processes at detector level, and the relative difference with respect to the SM.

Differential cross sections and ratios are shown in Figs. 6.61-6.64 for the ctG, in Figs. 6.65-6.68 for the cQq81, and in Figs. 6.69-6.72 for the ctq8. For the ratios, a linear fit is applied, to show the possible indication of a trend in the distribution.

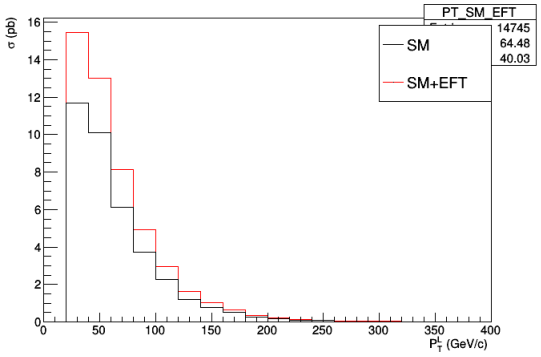

FIGURE 6.61: Differential cross section as a function of the transverse momentum of the leading lepton, in the semi-leptonic state, for the ctG coefficient.

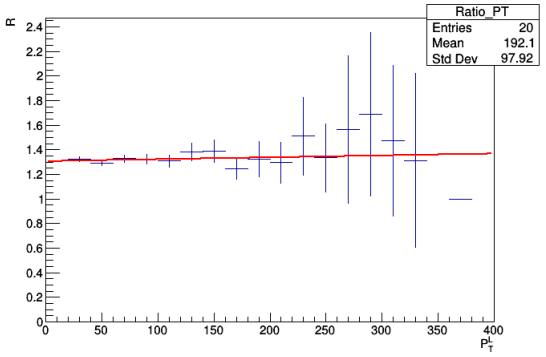

FIGURE 6.62: Cross section ratio as a function of the transverse momentum of the leading lepton, in the semi-leptonic state, for the ctG coefficient.

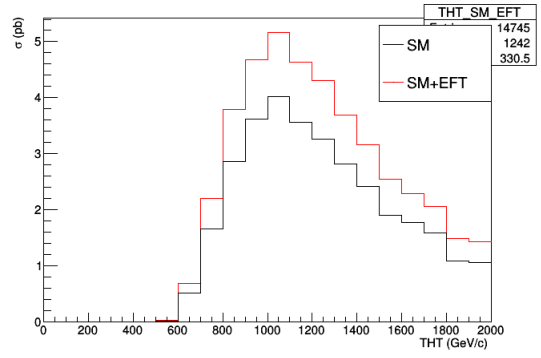

FIGURE 6.63: Differential cross section as a function of the THT variable, in the semi-leptonic state, for the ctG coefficient.

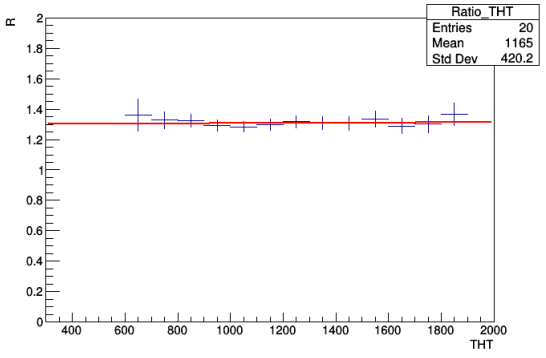

FIGURE 6.64: Cross section ratio as a function of the THT variable, in the semi-leptonic state, for the ctG coefficient.

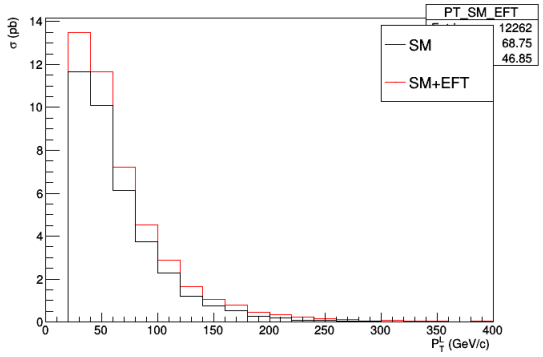

FIGURE 6.65: Differential cross section as a function of the transverse momentum of the leading lepton, in the semi-leptonic state, for the cQq81 coefficient.

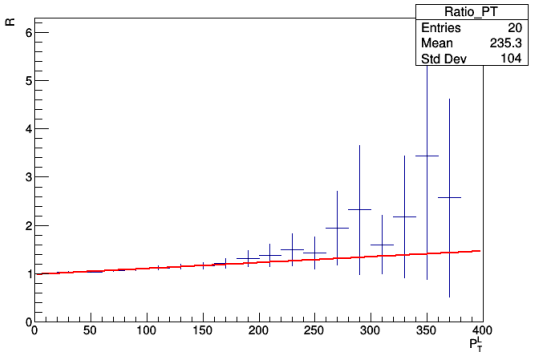

FIGURE 6.66: Cross section ratio as a function of the transverse momentum of the leading lepton, in the semi-leptonic state, for the cQq81 coefficient.

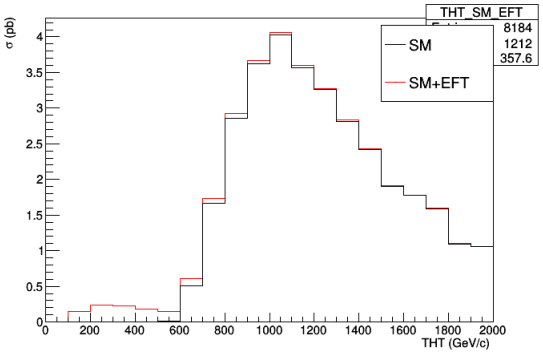

FIGURE 6.67: Differential cross section as a function of the THT variable, in the semi-leptonic state, for the cQq81 coefficient.

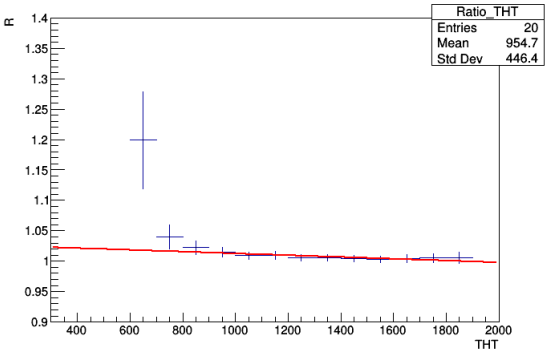

FIGURE 6.68: Cross section ratio as a function of the THT variable, in the semi-leptonic state, for the cQq81 coefficient.

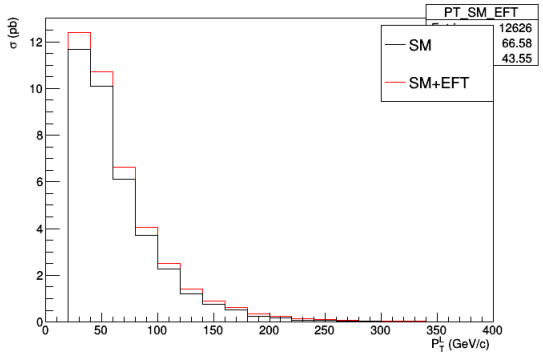

FIGURE 6.69: Differential cross section as a function of the transverse momentum of the leading lepton, in the semi-leptonic state, for the ctq8 coefficient.

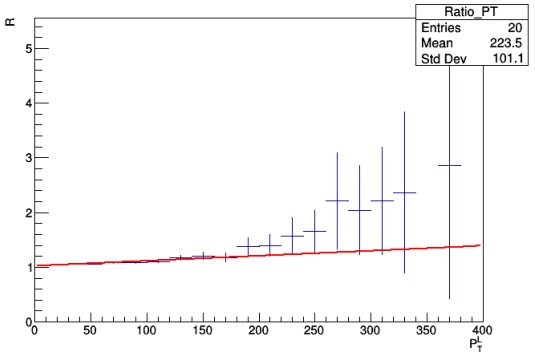

FIGURE 6.70: Cross section ratio as a function of the transverse momentum of the leading lepton, in the semi-leptonic state, for the ctq8 coefficient.

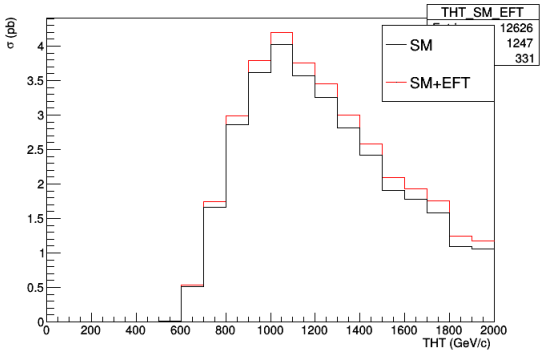

FIGURE 6.71: Differential cross section as a function of the THT variable, in the semi-leptonic state, for the ctq8 coefficient.

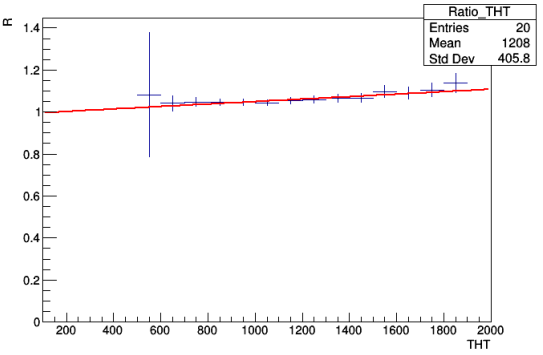

FIGURE 6.72: Cross section ratio as a function of the THT variable, in the semi-leptonic state, for the ctq8 coefficient.

6.2.3 Dileptonic process

We defined this channel the same way as we did for the dileptonic channel at particle level.

The differential cross-section after the event selection for SM and EFT for this channel are summarized in Table 6.7

Process	Cross-section (pb)	Difference relative to SM (in per mille)
SM	5.85	-
ctG=1	1.98	338.46
cQq81=5	0.54	92.31
ctq8=5	0.52	88.89

TABLE 6.7: Cross-section for the dileptonic channel for the different processes at detector level, and the relative difference with respect to the SM.

Differential cross sections and ratios are shown in Figs. 6.73-6.76 for the ctG, in Figs. 6.77-6.80 for the cQq81, and in Figs. 6.81-6.84 for the ctq8. For the ratios, a linear fit is applied, to show the possible indication of a trend in the distribution.

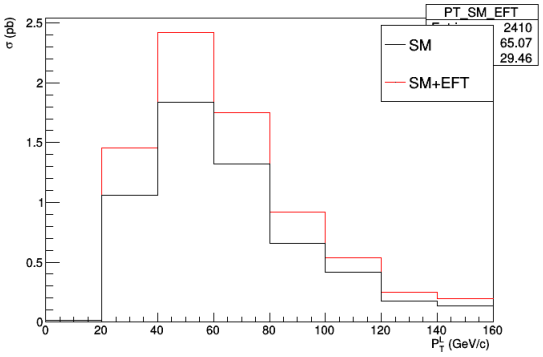

FIGURE 6.73: Differential cross section as a function of the transverse momentum of the leading lepton, in the dileptonic state, for the ctG coefficient.

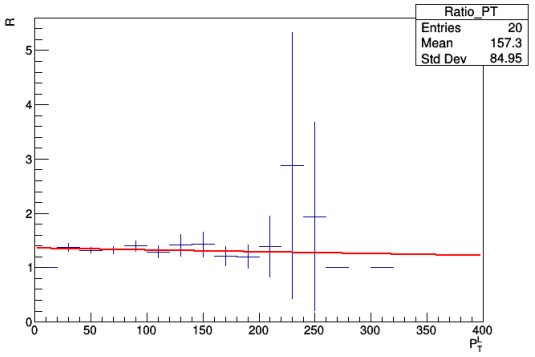

FIGURE 6.74: Cross section ratio as a function of the transverse momentum of the leading lepton, in the dileptonic state, for the ctG coefficient.

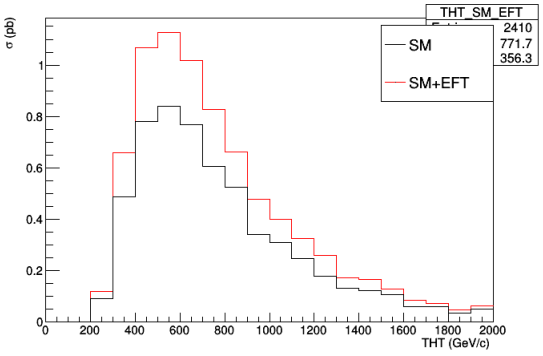

FIGURE 6.75: Differential cross section as a function of the THT variable, in the dileptonic state, for the ctG coefficient.

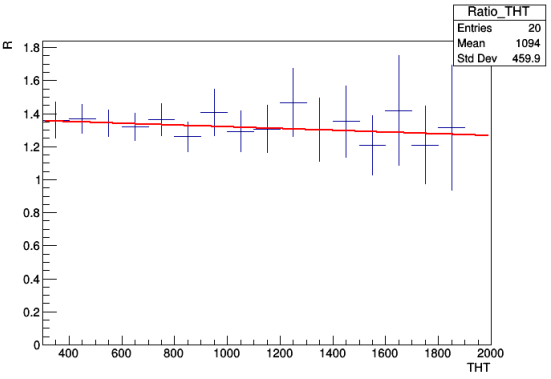

FIGURE 6.76: Cross section ratio as a function of the THT variable, in the dileptonic state, for the ctG coefficient.

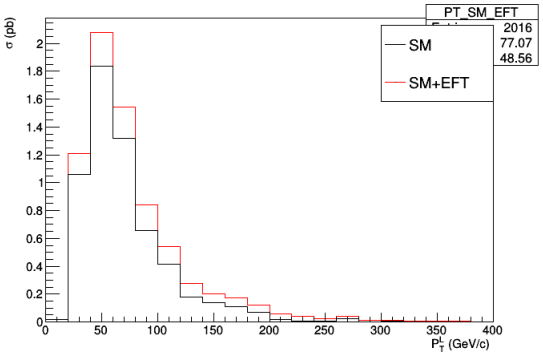

FIGURE 6.77: Differential cross section as a function of the transverse momentum of the leading lepton, in the dileptonic state, for the cQq81 coefficient.

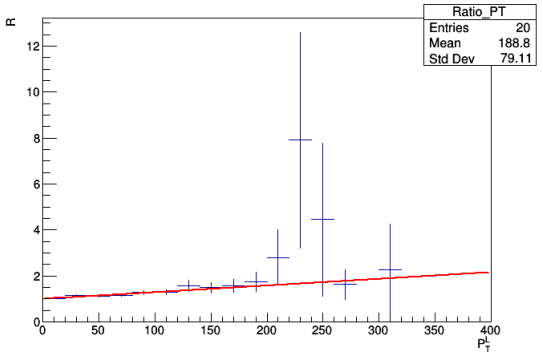

FIGURE 6.78: Cross section ratio as a function of the transverse momentum of the leading lepton, in the dileptonic state, for the cQq81 coefficient.

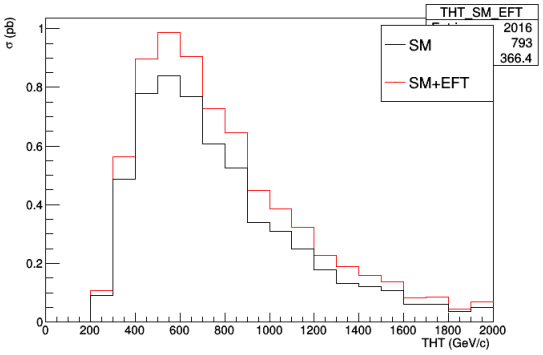

FIGURE 6.79: Differential cross section as a function of the THT variable, in the dileptonic state, for the cQq81 coefficient.

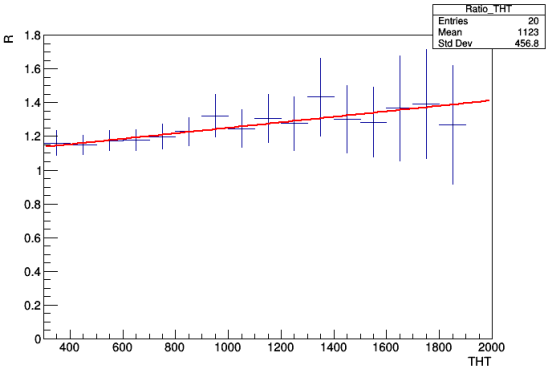

FIGURE 6.80: Cross section ratio as a function of the THT variable, in the dileptonic state, for the cQq81 coefficient.

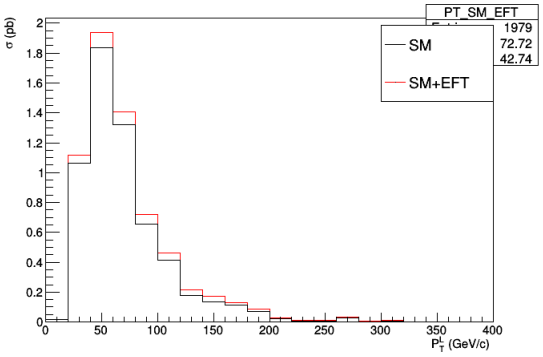

FIGURE 6.81: Differential cross section as a function of the transverse momentum of the leading lepton, in the dileptonic state, for the ctq8 coefficient.

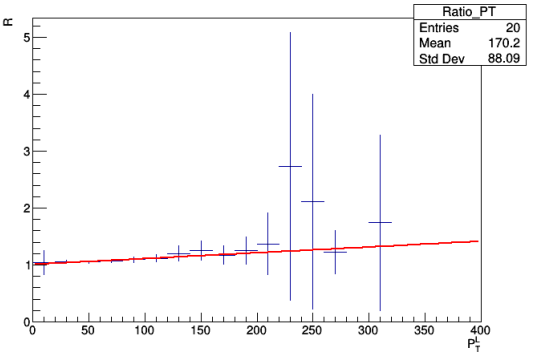

FIGURE 6.82: Cross section ratio as a function of the transverse momentum of the leading lepton, in the dileptonic state, for the ctq8 coefficient.

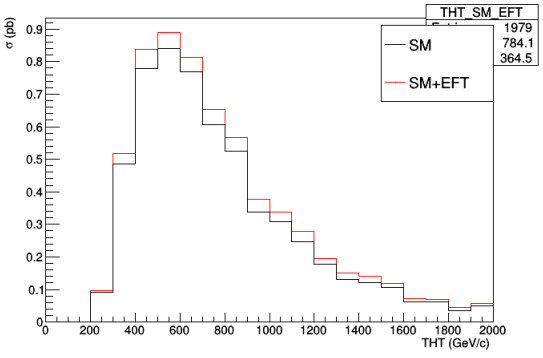

FIGURE 6.83: Differential cross section as a function of the THT variable, in the dileptonic state, for the ctq8 coefficient.

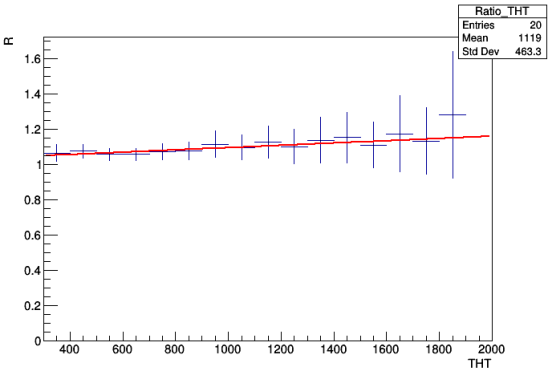

FIGURE 6.84: Cross section ratio as a function of the THT variable, in the dileptonic state, for the ctq8 coefficient.

Chapter 7

Discussion and considerations

The discussion of the results obtained in the previous chapter are based on:

- showing which are the relevant coefficients that might be constrained by $t\bar{t}$ analysis, i.e. the comparison of the observed to expected events;
- evaluate the relative effects obtained in each channel;
- considering the ratio of the differential distributions for relevant variables, to see those which show a significant trend which might enable a stronger constraint on the Wilson coefficients.

The EFT contribution on the $t\bar{t}$ differential cross-section depends on the Wilson coefficient that we chose. Analysing the total EFT cross-section, which includes the interference and quadratic term for each Wilson coefficient with a value of 1, we can see that the ones that give the higher contribution to the cross-section are:

- ctG with an EFT cross-section of 159 pb, corresponding to a relative difference of ≈ 300 per mille with respect to the SM cross-section alone;
- cQq81, with an EFT cross-section of 7.6 pb, corresponding to a relative difference of ≈ 14 per mille;
- ctq8, with an EFT cross-section of 7.6 pb, corresponding to a relative difference of ≈ 14 per mille;

Due to the fact that these coefficients are the ones that have a higher contribution, they might be better constrained by a complete $t\bar{t}$ analysis.

The Wilson coefficients cQq81 and ctq8 contribute less to the cross-section that the ctG coefficients. To emphasize their contribution we calculated the effect of setting the coefficient values equal to 5, instead of 1. In this case the EFT cross-section for both cQq81 and ctq8 would become 63 pb, with a relative increase with respect to the SM cross-section of ≈ 120 per mille. Clearly, a complete $t\bar{t}$ analysis would be able to impose weaker constraints on cQq81 and ctq8, with respect to those possible for ctG; similarly allowed intervals for cQq81 and ctq8 values will be wider than those possible for ctG.

Based on the analysis made in the three different channels we can see that there are different effects in each channel, and also that each one has different kinematic variables which are most relevant. We notice that different results are obtained at particle level and at detector level. After applying all the requirements and comparing the cross-sections for selected events we see that these values are typically largest in the case of the all-hadronic channel. Considering both levels, we obtain for the all-hadronic channel at detector level an event cross-section of ≈ 65 pb for the SM, and of ≈ 22 pb for the EFT model including the ctG coefficient; at particle level these two values are ≈ 49 pb and ≈ 16 pb, respectively. This means that a channel selection based on the same thresholds for p_T and η of jets/e/μ is more efficient when considering detector-level quantities. The cross-section values for the semi-leptonic channel are slightly smaller than for the all-hadronic one, while their are about half for the dilepton channel, both at particle and detector level. For all channels, the ctG coefficients is the one that has the largest contribution, with ctq8 and cQq81 having a smaller and similar contribution.

Based on the histograms that we made of the differential cross-section as a function of the different variables, we calculate the ratio between SMEFT and SM, as shown in Eq. 5.5 and we do a linear fit to see more clearly if there is a trend which will help us to constrain the Wilson coefficients.

At particle level for the ctG variable in the hadronic channel, we can see that:

- there is a trend in jet multiplicity: the fitted line decreases with the increasing number of jets;
- for the p_T of the leading jet, the ratio slightly increases at large values of p_T;
- for the scalar sum THT, the ratio does not show a significant trend

This suggest us that in order to better constrain the ctG coefficient in a possible analysis one could concentrate on low values for the jet multiplicity, large values for the leading-jet p_T and large values for THT. Of course this consideration will need to be re-evaluated when a complete analysis accounts also for the behavior of background events.

Based on the trend shown in ratios for the cQq81 and ctq8 in the all-hadronic channel we could have a better constrain if we required low jet multiplicity, higher values of p_T of the leading jet and THT. In the semi-leptonic channel for this three coefficients we can see that larger values of THT and of the leading lepton p_T give a better sensitivity, meaning that the coefficients can be better constrained selecting this kinematical regions. In the dileptonic channel we see that for the THT variable the fit line that we calculate is almost flat, meaning that there is no trend in this variable, and nothing to be gained by selecting a particular region. For the p_T of the leading lepton there is a small trend, and something can be gained by selecting high values.

At detector level, we obtain for the ctG coefficient results similar to what we seen at particle level: a slightly better sensitivity at a low number of jets, at high values for the leading jet p_T. For the cQq81 and ctq8 coefficients, the number of jets and the p_T of the leading jet have a similar behaviour to what observed at particle level, while the THT variable does not help in the hadronic channel, since the linear form of the ratio is quite flat. The same happens in the semi-leptonic channel where the THT variable does not help much. In the dileptonic case some gain is possible for the cQq81 and ctq8 coefficient by selecting large values of leading lepton p_T and for the THT variables, while for the ctG coefficient these two variables does not help much.

Chapter 8

Conclusions

Effective field theories help us to search for new particles, by characterising corrections to the Lagrangian and the cross-section of the SM in order to construct the SMEFT framework. In this case the SM Lagrangian is extended to higher order operators, and will depend on the Wilson coefficients that parametrize the strength of new physics interactions. In this project we based our analysis on $t\bar{t}$ production, since the top quark is possibly the SM state that is closest to the new physics sector, due to the fact that it is the heaviest particle, and the one that has the largest Yukawa coupling.

We perform an analysis at particle and detector level for the three decay channels of $t\bar{t}$: all-hadronic, semi-leptonic and dileptonic. We have generated 100,000 events for the SM and EFT productions with the most relevant coefficients: ctG with a value of 1, cQq81 and ctq8 with a value of 5, which give larger contributions to the cross-section. We analysed the differential cross section as a function of the different kinematic variables to see which regions will help us constrain the Wilson coefficients.

We conclude that for the ctG, cQq81 and ctq8 coefficients in the all-hadronic channel we should concentrate in the region of low jet multiplicity and large values of leading jet p_T and THT. Instead for the semi-leptonic channel we could obtain a better sensitivity if we focus in the regions with high leading lepton p_T and THT. In the dileptonic case we can see that for the THT variable we cannot gain anything. In order to improve the analysis we can study other variables that will help to obtain a larger contribution of the EFT cross-section, taking into account also the background events, to see which are the regions that will help to constrain more each Wilson coefficient.

Bibliography

[1] J. Bernstein. *Spontaneous symmetry breaking, gauge theories, the Higgs mechanism and all that. Rev. Mod. Phys. 46 (1974) 7.* doi: 10.1103/RevModPhys.46.7. URL https://link.aps.org/doi/10.1103/RevModPhys.46.7.

[2] C. Weinheimer and K. Zuber. *Neutrino masses. Annalen der Physik 525 (2013) 565.*

[3] N. Arkani-Hamed, S. Dimopoulos, and G. Dvali. *The hierarchy problem and new dimensions at a millimeter. Physics Letters B 429 (1998) 263.*

[4] L. Moreels. *Search for stop quarks using the matrix element method at the LHC*. Master's thesis, Vrije U., Brussels, (2013). URL http://iihe.ac.be/publications/Stop_search_with_MEM_at_LHC_lmoreels.pdf.

[5] CMS Collaboration. *Search for top squarks and dark matter particles in opposite-charge dilepton final states at $\sqrt{s} = 13$ TeV. Phys. Rev. D 97 (2018) 032009.* doi: 10.1103/PhysRevD.97.032009.

[6] I. Brivio and M. Trott. *The Standard Model as an effective field theory. Physics Reports 793 (2019) 1.*

[7] The LHC Top working group. *Supersymmetric glue: the search for gluinos.* URL arXiv:1802.07237.

[8] F. Pandolfi. *Search for the Standard Model Higgs Boson in the H ZZ l+ l-qq Decay Channel at CMS.* Springer Science & Business Media, (2013).

[9] P. Langacker. *The standard model and beyond.* CRC press, (2017).

[10] ATLAS Collaboration. *Observation of a new particle in the search for the Standard Model Higgs boson with the ATLAS detector at the LHC*. Phys. Lett. B 716 (2012) 1, doi: 10.1016/j.physletb.2012.08.020.

[11] CMS Collaboration. *Observation of a new boson at a mass of 125 GeV with the CMS experiment at the LHC.* Phys. Lett. B 716 (2012) 30, doi: 10.1016/j.physletb.2012.08.021.

[12] D. Spergel and et al. *First-year Wilkinson Microwave Anisotropy Probe (WMAP)* observations: determination of cosmological parameters. The Astrophysical Journal Supplement Series 148 (2003) 175.*

[13] D. Clowe and et al. *A direct empirical proof of the existence of dark matter. The Astrophysical Journal Letters 648 (2006) L109.*

[14] *Dark Energy, Dark Gravity.* https://darkmatterdarkenergy.com/tag/planck/. Accessed: 2020-05-27.

[15] L. Moreels. *Search for stop quarks using the matrix element method at the LHC*. Master's thesis, Vrije U., Brussels, (2013). URL http://iihe.ac.be/publications/Stop_search_with_MEM_at_LHC_lmoreels.pdf.

[16] S. Moortgat. *When charm and beauty adjoin the top. First measurement of the cross section of top quark pair production with additional charm jets with the CMS experiment.*, PhD thesis (2019). URL https://cds.cern.ch/record/2676133.

[17] B. Grzadkowski et al. *Dimension-Six Terms in the Standard Model Lagrangian. JHEP 10 (2010) 085.* doi: 10.1007/JHEP10(2010)085.

[18] LHC Top Working Group. *Interpreting top-quark LHC measurements in the standard-model effective field theory*. arxiv:1802.07237 (2018).

[19] CMS Collaboration. *Public CMS luminosity information*, (2017). URL https://twiki.cern.ch/twiki/bin/view/CMSPublic/LumiPublicResult.

[20] P. De Aquino. *Beyond standard model phenomenology at the LHC*. Springer Science & Business Media, (2013).

[21] R. Atkin. *Review of jet reconstruction algorithms. J. Phys. Conf. Ser. (2015) 1.* doi: 10.1088/1742-6596/645/1/012008.

[22] M. Cacciari, G. P. Salam, and G. Soyez. *The Anti-k(t) jet clustering algorithm. JHEP 04 (2008) 63.* doi: 10.1088/1126-6708/2008/04/063.

[23] C. Lefevre. *The CERN accelerator complex*, (2008). URL http://cds.cern.ch/record/1260465Web. Accessed: 2020-05-10.

[24] CMS Collaboration. *Search for new physics with the M_{T2} variable in all-jets final states produced in pp collisions at $\sqrt{s} = 13$ TeV*. JHEP 10 (2016) 006, doi: 10.1007/JHEP10(2016)006.

[25] CMS Collaboration. *CMS Physics: Technical Design Report Volume 1: Detector Performance and Software.* Technical report, CMS-TDR-008-1, (2006).

[26] CMS Collaboration. *The CMS Experiment at the CERN LHC*. JINST 3 (2008) S08004, doi: 10.1088/1748-0221/3/08/S08004.

[27] M. Cacciari and et al. *Top-pair production at hadron colliders with next-to-next-to-leading logarithmic soft-gluon resummation*. *Phys. Lett. B 710 (2012) 612*. doi: 10.1016/j.physletb.2012.03.013.

[28] CMS Collaboration. *Measurement of the cross section for top quark pair production in association with a W or Z boson in proton-proton collisions at* $\sqrt{s} = 13$ *TeV*. JHEP (2018) 11.

[29] ATLAS Collaboration. *Search for four-top-quark production in the single-lepton and opposite-sign dilepton final states in pp collisions at s= 13 TeV with the ATLAS detector*. Phys. Rev. D 99 (2019) 052009.

[30] CMS Collaboration. *Measurements of* tt^- *differential cross sections in proton-proton collisions at* $\sqrt{s}$*= 13 TeV using events containing two leptons*. JHEP 02 (2019) 149.

[31] CMS Collaboration. *Measurement of the top quark polarization and t* t^- *spin correlations using dilepton final states in proton-proton collisions at* $\sqrt{s}$*= 13 TeV*. Phys. Rev. D 100 (2019) 072002.

[32] CMS collaboration. *Measurement of top quark pair production in association with a Z boson in proton-proton collisions at* $\sqrt{s} = 13$ *TeV. JHEP 03 (2020) 056.*

[33] CMS Collaboration. *Search for new physics in top quark production in dilepton final states in proton-proton collisions at* $\sqrt{s} = 13$ *TeV*. Eur. Phys. J. C 79 (2019) 886.

[34] F. Maltoni and T. Stelzer. *MadEvent: Automatic event generation with MadGraph. JHEP0302 (2003) 027.*

[35] T. Sjöstrand, S. Mrenna, and P. Skands. *PYTHIA 6.4 physics and manual. JHEP 0605 (2006) 026.*

[36] E. Conte, B. Fuks, and G. Serret. *MadAnalysis 5, a user-friendly framework for collider phenomenology. Computer Physics Communications 184 (2013) 222.*

[37] M. Selvaggi. *DELPHES 3: A modular framework for fast-simulation of generic collider experiments*. *J. Phys. Conf. Ser. 523 (2014)*. doi: 10.1088/1742-6596/523/1/012033.

[38] CMS Collaboration. *Particle-flow reconstruction and global event description with the CMS detector. JINST 12 (2017) P10003.*

List of Figures

List of Tables